

Angular Momentum Transport by Acoustic Modes Generated in the Boundary Layer I: Hydrodynamical Theory and Simulations.

Mikhail A. Belyaev¹ & Roman R. Rafikov¹ & James M. Stone¹

ABSTRACT

The nature of angular momentum transport in the boundary layers of accretion disks has been one of the central and long-standing issues of accretion disk theory. In this work we demonstrate that acoustic waves excited by supersonic shear in the boundary layer serve as an efficient mechanism of mass, momentum and energy transport at the interface between the disk and the accreting object. We develop the theory of angular momentum transport by acoustic modes in the boundary layer, and support our findings with 3D hydrodynamical simulations, using an isothermal equation of state. Our first major result is the identification of three types of global modes in the boundary layer. We derive dispersion relations for each of these modes that accurately capture the pattern speeds observed in simulations to within a few percent. Second, we show that angular momentum transport in the boundary layer is intrinsically nonlocal, and is driven by radiation of angular momentum away from the boundary layer into both the star and the disk. The picture of angular momentum transport in the boundary layer by waves that can travel large distances before dissipating and redistributing angular momentum and energy to the disk and star is incompatible with the conventional notion of local transport by turbulent stresses. Our results have important implications for semianalytical models that describe the spectral emission from boundary layers.

Subject headings: accretion, accretion disks – hydrodynamics — waves – instabilities

1. Introduction

Understanding the structure and dynamics of the boundary layer (BL) is one of the outstanding theoretical problems in accretion disk theory. We define the BL as the thin transitional region where the disk attaches to the star, gas slows down from the orbital to the stellar rotation velocity, and $d\Omega/d\varpi > 0$ (Ω is the angular velocity of the fluid and ϖ is the cylindrical radius). In this work, we do not differentiate between the different types of accreting objects (a neutron star, a white dwarf, or a young star), as long as they have a surface. This assumes that the compact object has a weak enough magnetic field that the disk extends all the way down to the surface of the star without

¹Department of Astrophysical Sciences, Princeton University, Ivy Lane, Princeton, NJ 08540; rrr@astro.princeton.edu

being disrupted and channeled to the magnetic poles. The criteria for this to occur is that the magnetic pressure should be less than the ram pressure of the gas at the surface of the star (Ghosh & Lamb 1978).

Within the BL, material slows down from the Keplerian rotational velocity to the rotational velocity inside the star. Since the radial width of the BL is significantly less than that of the star, this implies that the BL is a region of intense shear. In fact, the rate of energy dissipation inside the BL is expected to be as high as for the rest of the disk combined (Kluźniak 1987), resulting in intense heating of the gas.

An open question in BL theory is the mechanism of angular momentum transport. Due to a rising rotation profile, the BL is linearly stable to the magnetorotational instability (MRI) which is responsible for accretion in the disk (Balbus & Hawley 1991). Indeed, Pessah & Chan (2012) has shown that if $d\Omega/d\varpi > 0$, then the stresses due to a sheared magnetic field are inefficient at transporting angular momentum and oscillate about zero. Thus, some other mechanism must be responsible for angular momentum transport within the BL. As we have previously shown in Belyaev et al. (2012), a likely candidate for this mechanism is excitation of acoustic waves in the BL accompanied by radiation of angular momentum away from the layer. This acoustic radiation arises due to sonic instabilities in the BL, which are a type of shear instability akin to the Papaloizou-Pringle instability (Papaloizou & Pringle 1984; Narayan et al. 1987) that operate in supersonic flows (Glatzel 1988; Belyaev & Rafikov 2012).

The focus of our present work will be the detailed description of acoustic modes in the BL and their relation to angular momentum transport and mass. We will study these modes both theoretically by solving for their dispersion relation and computationally with 2D, 3D unstratified, and 3D stratified hydro simulations of the BL with an isothermal equation of state.

Understanding the physics of acoustic modes is an important step towards understanding the temporal variability in the BL and constructing semianalytic models of BL spectra. Currently, virtually all semianalytic models of the BL assume that angular momentum transport is mediated by local turbulent stresses and adopt an effective α -prescription based on Navier-Stokes viscosity (Popham & Narayan 1995; Inogamov & Sunyaev 1999; Piro & Bildsten 2004a). We argue, however, that angular momentum in the BL is transported by global waves, rather than local turbulence. These waves can potentially travel long distances before dissipating, meaning that angular momentum and energy transport is inherently nonlocal and cannot be well-described by any model based on a local anomalous viscosity.

The paper is organized as follows. In §2, we describe the model setup and numerical methods that we use for studying the BL, and in §3 we provide a general overview of our simulation results. We find that sonic instabilities are a ubiquitous outcome in our simulations and excite acoustic modes that radiate angular momentum into both the star and the disk. In §4, we show that the acoustic modes observed in simulations have a dispersion relation that is well-described by a few simple modifications to the dispersion relation of the supersonic vortex sheet (Miles 1958; Gerwin

1968; Belyaev & Rafikov 2012). In §5, we show that radiation from $k_z = 0$ acoustic modes entirely accounts for the angular momentum transport in our simulations and discuss the implications of this result for semi-analytic models of the BL. Finally, in §6 we discuss the effects of disk stratification in the z -direction on acoustic modes and angular momentum transport, and we find that stratification makes no fundamental difference to our results.

2. Numerical Model

2.1. Governing Equations

For our simulations we use the Godunov code Athena (Stone et al 2008) to solve the Euler equations of fluid dynamics in cylindrical geometry with an isothermal equation of state. These equations are

$$\frac{\partial \rho}{\partial t} + \nabla \cdot (\rho \mathbf{v}) = 0, \quad (1)$$

$$\frac{\partial(\rho \mathbf{v})}{\partial t} + \nabla \cdot (\rho \mathbf{v} \mathbf{v}) + \nabla P + \rho \nabla \Phi = 0, \quad (2)$$

$$P = \rho s^2. \quad (3)$$

Here, \mathbf{v} is the velocity, ρ is either the density (3D) or the surface density (2D), P is the pressure, Φ is the gravitational potential, and s is the sound speed. We also use ϖ throughout this work to denote the cylindrical radius.

2.2. Nondimensional Units

Our initial setup, described in more detail below, consists of a star which attaches to a constant density disk via a thin interfacial region. Following the convention of Belyaev et al. (2012), we nondimensionalize quantities by setting the radius of the star to $\varpi_\star = 1$, which defines a unit of length, the Keplerian angular velocity to $\Omega_K(\varpi_\star) = 1$, which defines a unit of time, and $\rho = 1$ within the disk, which defines a characteristic density. Expressed in these units, the orbital timescale at the surface of the star is $P_K = 2\pi$.

We also define a characteristic Mach number as $M \equiv 1/s$, which is the true Mach number of the flow in the disk at the surface of the star, since $V_K(\varpi_\star) = 1$. For a given set of initial conditions, the Mach number is the sole *physical* parameter that determines the time-evolution of the system (Belyaev et al. 2012), assuming an isothermal equation of state. Thus, the solutions to equations (1)-(3) form a one-parameter family in the Mach number. However, in practice there are also *numerical* parameters, e.g. the size of the simulation domain, that influence the outcome of a simulation.

2.3. Gravitational Potential

We take the gravitational potential to be fixed throughout the course of a simulation. This amounts to ignoring the self-gravity of the outer layers of the star (Cowling’s approximation, Cowling (1941)), which was discussed in the context of the BL in Belyaev & Rafikov (2012).

We run both vertically stratified and unstratified simulations. For vertically unstratified runs, we use the cylindrically symmetric potential

$$\Phi = -\frac{1}{\varpi}, \quad (4)$$

whereas for vertically stratified runs, we use the point mass potential

$$\Phi = -\frac{1}{\sqrt{\varpi^2 + z^2}}, \quad (5)$$

where z is the height above the midplane.

2.4. Initial Rotation Profile

Initially, the star attaches to the disk via a thin interface, inside of which the rotational velocity, v_ϕ , rises very nearly linearly from zero (the velocity in the star) to the Keplerian orbital velocity (the velocity in the disk). The initial rotation profile is given by

$$\Omega(\varpi) = \begin{cases} 0 & \varpi < 1 - \frac{\delta_{BL,0}}{2} & \text{“star”} \\ \varpi^{-3/2} \left(\frac{\varpi-1}{\delta_{BL,0}} + \frac{1}{2} \right) & 1 - \frac{\delta_{BL,0}}{2} \leq \varpi \leq 1 + \frac{\delta_{BL,0}}{2} & \text{“interface”} \\ \varpi^{-3/2} & \varpi > 1 + \frac{\delta_{BL,0}}{2} & \text{“disk”} \end{cases}, \quad (6)$$

and is the same as in Belyaev et al. (2012) (see their Figure 1). For all our runs, we use $\delta_{BL,0} = .01$, so the interface is as narrow as possible, while still being resolved with ~ 10 cells. Our results are independent of $\delta_{BL,0}$, since over the course of a simulation, the interface thickens into a self-consistent BL with width $\gg \delta_{BL,0}$ due to angular momentum transport by acoustic modes.

2.5. Initial Density and Pressure Profiles

The initial pressure profile is specified everywhere throughout the domain through the equation of hydrostatic equilibrium

$$\frac{1}{\rho} \frac{\partial P}{\partial \varpi} = -\frac{\partial \Phi}{\partial \varpi} + \Omega^2 \varpi, \quad (7)$$

$$\frac{1}{\rho} \frac{\partial P}{\partial z} = -\frac{\partial \Phi}{\partial z}. \quad (8)$$

The density is directly proportional to the pressure and is related to it through the equation of state (3).

For the 2D and 3D unstratified simulations, the initial density is $\rho(\varpi, t = 0) = 1$ within the disk, and $\rho(\varpi, t = 0) = \exp[-\Phi(\varpi)/s^2]$ within the star, where $\Omega = 0$. For the stratified simulations, these expressions are also accurate for the midplane density, $\rho_0(\varpi, t = 0) \equiv \rho(\varpi, z = 0, t = 0)$, as long as we use the midplane potential $\Phi_0(\varpi) \equiv \Phi(\varpi, z = 0)$. The initial density throughout the simulation domain for a stratified simulation can be expressed in terms of the initial midplane density as $\rho(\varpi, z, t = 0) = \rho_0(\varpi, t = 0) \exp[-(\Phi(\varpi, z) - \Phi_0(\varpi))/s^2]$. This formula is valid everywhere, including the interfacial region, since we have rotation on cylinders throughout the simulation domain, i.e. Ω is a function only of ϖ (equation [6]).

2.6. Boundary Conditions

In all of our simulations, we use periodic boundary conditions (BCs) in the ϕ direction and “do-nothing” BCs in the ϖ direction. The “do-nothing” BC simply means that all fluid quantities retain their initial, equilibrium values for the duration of the simulation at the inner and outer ϖ -boundaries. A “do-nothing” BC in ϖ is advantageous to an outflow BC, especially at the inner edge of the domain inside the star, since it prevents a systematic change in the density profile over the course of the simulation due to small deviations from equilibrium. A “do-nothing” BC is also advantageous to a reflecting BC, since it allows sound waves to leave the domain. However, a “do-nothing” BC does not absorb radiation perfectly (neither does an outflow BC), and there is some partial reflection of waves from the radial boundaries, although the reflection coefficient is significantly less than unity (see §5.1.2).

For the 3D unstratified and stratified simulations we use periodic BCs in the z -direction. The reason for using periodic BCs in the z -direction as opposed to outflow BCs, even in the stratified case, is that it is hard to achieve a good numerical equilibrium with outflow BCs. The application of outflow BCs is potentially more straightforward in spherical geometry (in the θ -direction), since in that case the gravity vector is parallel to the θ -boundary.

2.7. Initial Perturbations and Burn-In

Although we initialize our density and pressure profiles to satisfy the equations of hydrostatic equilibrium (equations [7] and [8]), we find that we need to burn-in our simulations for $t \sim 100$ to let any initial transients damp out and achieve a good numerical hydrostatic equilibrium. This burn-in procedure was previously used by Armitage (2002) in studying the BL, and we find it easier than setting up an exact numerical equilibrium (Zingale et al. 2002).

After the burn-in period, we introduce random perturbations to v_ϖ of amplitude $\delta v_\varpi \sim .001$

in the region $\varpi > 1$. These random perturbations to the radial velocity seed the sonic instability and facilitate the growth of acoustic modes. The reason for only introducing perturbations in the region $\varpi > 1$ is that waves traveling from high density to low density regions amplify by a factor of $\rho^{-1/2}$ to conserve energy. Since the density in the star is up to 10^6 times higher than that in the disk, we want to avoid any transient waves that amplify as they travel out of the star and into the disk.

2.8. Simulation-Specific Parameters

Table 1 lists the simulation specific-parameters for each of our runs. Typically, our simulations are run until a time of $t \approx 400 - 600$ (70 – 100 orbits at the inner edge of the disk), where $t = 0$ corresponds to the time when the random perturbations are introduced to the radial velocity. We find that this is long enough for the boundary layer to widen to an approximately steady-state width, after an initial period of rapid growth. Some of our simulations are run for over 100 orbits, and we observe little change in the behavior of the fluid in the vicinity of the BL or in the width of the boundary layer at the end of these runs as compared to our typical ones.

The four most important parameters we vary from simulation to simulation are dimensionality (2D or 3D), Mach number ($M = 6$ or $M = 9$), stratification in the z -direction (unstratified or stratified), and the ϕ extent of the simulation domain. Comparing the effects of dimensionality and stratification across simulations with all other parameters held constant allow us to probe how the thickness of the disk affects the dynamics of the system. Varying the Mach number gives us a handle on how the phenomena we discuss translate over to astrophysical systems which tend to have higher Mach numbers (e.g. $M \sim 100$ for white dwarfs). Finally, changing the ϕ extent of the simulation domain gives us a measure of control over the wavelength of the dominant modes present in the box, allowing us to probe the dispersion relation for our model (§4).

3. General Overview

We now present a general overview of our simulation results that will frame the discussion throughout the paper.

3.1. Notation for Measured Quantities

We begin by introducing some notation, regarding how simulation quantities are measured. For 3D simulations, we define a z -averaged density as

$$\Sigma(\varpi, \phi) \equiv \frac{1}{\Delta z} \int dz \rho, \quad (9)$$

| label | dimension | M | stratified | ϖ -range | ϕ -range | z -range | $N_\varpi \times N_\phi \times N_z$ |
|-------|-----------|-----|------------|-----------------|----------------|---------------|-------------------------------------|
| 3D6a | 3D | 6 | no | (.7, 2.5) | (0, 2π) | (-1/12, 1/12) | $2048 \times 2048 \times 32$ |
| 3D6b | 3D | 6 | no | (.7, 2.5) | (0, 2π) | (-1/6, 1/6) | $2048 \times 2048 \times 64$ |
| 3D6c | 3D | 6 | yes | (.7, 2.5) | (0, 2π) | (-1/3, 1/3) | $1536 \times 1536 \times 128$ |
| 3D6d | 3D | 6 | no | (.7, 2.5) | (0, $\pi/3$) | (-1/12, 1/12) | $2048 \times 384 \times 32$ |
| 3D9a | 3D | 9 | no | (.85, 2.5) | (0, 2π) | (-1/18, 1/18) | $2048 \times 2048 \times 32$ |
| 3D9b | 3D | 9 | no | (.85, 2.5) | (0, 2π) | (-1/9, 1/9) | $2048 \times 2048 \times 64$ |
| 3D9c | 3D | 9 | yes | (.85, 2.5) | (0, 2π) | (-2/9, 2/9) | $1536 \times 1536 \times 128$ |
| 3D9d | 3D | 9 | no | (.85, 2.5) | (0, $\pi/3$) | (-1/18, 1/18) | $2048 \times 384 \times 32$ |
| 3D9e | 3D | 9 | no | (.85, 2.5) | (0, $2\pi/7$) | (-1/18, 1/18) | $2048 \times 384 \times 32$ |
| 3D9f | 3D | 9 | no | (.85, 2.5) | (0, $2\pi/7$) | (-1/18, 1/18) | $2048 \times 384 \times 64$ |
| 2D6a | 2D | 6 | – | (.7, 2.5) | (0, 2π) | – | $2048 \times 2048 \times 1$ |
| 2D6b | 2D | 6 | – | (.7, 2.5) | (0, $\pi/2$) | – | $2048 \times 512 \times 1$ |
| 2D6c | 2D | 6 | – | (.7, 2.5) | (0, $\pi/4$) | – | $2048 \times 256 \times 1$ |
| 2D6d | 2D | 6 | – | (.7, 2.5) | (-.4, .4) | – | $2048 \times 512 \times 1$ |
| 2D9a | 2D | 9 | – | (.85, 2.5) | (0, 2π) | – | $4096 \times 4096 \times 1$ |
| 2D9b | 2D | 9 | – | (.85, 2.5) | (0, $\pi/2$) | – | $4096 \times 1024 \times 1$ |
| 2D9c | 2D | 9 | – | (.85, 2.5) | (0, $\pi/4$) | – | $4096 \times 512 \times 1$ |

Table 1: Summary of simulation parameters. The columns from left to right are: simulation label, dimensionality (2D or 3D), Mach number, stratification (yes = stratified, no = unstratified), radial extent of the simulation domain, azimuthal extent, vertical extent (only in 3D), number of grid points in the radial \times azimuthal \times vertical directions.

where the integral is performed over the entire z -extent of the domain, and Δz is the thickness of the simulation domain in the z direction. The ϕ -averaged density and perturbations to the density are then defined as

$$\Sigma_0(\varpi) \equiv \frac{1}{\Delta\phi} \int d\phi \Sigma \quad (10)$$

$$\delta\Sigma(\varpi, \phi) \equiv \Sigma - \Sigma_0 \quad (11)$$

$$\delta\rho(\varpi, \phi, z) \equiv \rho - \rho_0. \quad (12)$$

Next, we define the density-weighted averaging operator represented by a set of triangle brackets as

$$\langle f \rangle \equiv \frac{1}{\Delta z \Delta\phi \Sigma_0} \int dz d\phi \rho f. \quad (13)$$

In 2D, the density-weighted average is the same, except that there is no integral over the z -dimension. Sometimes, we perform density-weighted averages in only the z -direction so we also define the operation

$$\langle f \rangle_z \equiv \frac{1}{\Delta z \Sigma} \int dz \rho f. \quad (14)$$

Density-weighted averages are the proper way of measuring simulation quantities, since mathematically exact analogs to the fluid equations can be formulated in terms of them (Balbus & Papaloizou 1999). For instance, one-dimensional forms for the continuity and angular momentum transport equations are

$$\frac{\partial \Sigma_0}{\partial t} + \frac{1}{\varpi} \frac{\partial}{\partial \varpi} (\varpi \Sigma_0 \langle v_\varpi \rangle) = 0 \quad (15)$$

$$\frac{\partial}{\partial t} (\varpi^2 \Sigma_0 \Omega) + \frac{1}{\varpi} \frac{\partial}{\partial \varpi} (\varpi^2 \Sigma_0 \langle v_\phi v_\varpi \rangle) = 0, \quad (16)$$

where we have assumed molecular viscosity is negligible in equation (16), and we have defined the angular velocity as

$$\Omega \equiv \frac{\langle v_\phi \rangle}{\varpi} \quad (17)$$

Equation (16) expresses angular momentum conservation and the second term is the divergence of the angular momentum flux,

$$F_L \equiv \varpi \Sigma_0 \langle v_\phi v_\varpi \rangle. \quad (18)$$

Throughout the paper we shall also refer to the angular momentum current, which is defined as

$$C_L \equiv 2\pi \varpi F_L. \quad (19)$$

The angular momentum current has the intuitive interpretation that the rate of change of angular momentum in an annular region is the difference in angular momentum current between the two edges of the annulus.

The angular momentum flux, F_L , can be decomposed into two parts (Balbus & Papaloizou 1999), which are the advective and stress terms

$$F_L = F_A + F_S \quad (20)$$

$$F_A \equiv \varpi^2 \Sigma_0 \Omega \langle v_\varpi \rangle \quad (21)$$

$$F_S \equiv \varpi \Sigma_0 \langle \delta v_\phi v_\varpi \rangle \quad (22)$$

$$\delta v_\phi \equiv v_\phi - \varpi \Omega. \quad (23)$$

These definitions are trivially generalized to 3D case by replacing Σ_0 with ρ_0 .

The advective term corresponds to angular momentum transport by the bulk motion of the fluid and can be written in terms of the mass accretion rate, \dot{M} , as

$$F_A = -\frac{\dot{M}}{2\pi \varpi} \varpi^2 \Omega \quad (24)$$

$$\dot{M} \equiv -2\pi \varpi \Sigma_0 \langle v_\varpi \rangle \quad (25)$$

The stress term, on the other hand, corresponds to angular momentum transport by turbulence and/or waves. In the standard α -viscosity treatment, the stress term is alternately written as (Shakura & Sunyaev 1973; Popham & Narayan 1995; Balbus & Papaloizou 1999)

$$F_S = \varpi \alpha \Sigma_0 s^2 \quad (26)$$

$$F_S = \varpi \alpha_\nu \Sigma_0 s^2 \left(-\frac{d \ln \Omega}{d \ln \varpi} \right) \quad (27)$$

$$F_S = \varpi \alpha_{\text{PN}} \Sigma_0 s^2 \left(-\frac{d \ln \Omega}{d \ln \varpi} \right) \left[1 + \left(\frac{s}{\Omega} \frac{d \ln P}{d \varpi} \right)^2 \right]^{-1/2}. \quad (28)$$

For any of these (or any other) α viscosity model to provide a good description of the BL, α should be approximately independent of ϖ . However, all conventional α viscosity models are based on the notion of *local* turbulent stresses. As we discuss in §5, in our BL simulations angular momentum transport is facilitated by waves not turbulence, and so is not well described by any local model.

3.2. Simulation Results

We now paint a picture of the typical evolution of one of our simulations. Due to the large shear in the interfacial region (§2.4), our initial rotation profile is unstable to the sonic instability (Glatzel 1988; Belyaev & Rafikov 2012; Belyaev et al. 2012). Consequently, acoustic modes are excited starting from the initial seed perturbations to the radial velocity (§2.7). The amplitude of these acoustic modes increases with time until $t \sim 60$ when the sonic instability saturates.

Around $t \sim 60$, there is typically a single mode present with a well-defined azimuthal pattern number, m , and pattern speed, Ω_P . This mode, which is discussed in detail in §4.2.1, has $\Omega_P \sim 1 - s$ and radiates angular momentum in the form of sound waves away from the vicinity of the interfacial region into both the disk and the star. This radiation of angular momentum causes the interfacial region to widen and drives accretion of material from the innermost portion of the disk onto the star.

Fig. 1a shows a radius-time image of Σ_0 for simulation 3D9a. From the image, it is clear that a gap in the density is opened up in the innermost portion of the disk starting at around $t \sim 60$, which is around the same time when the sonic instability saturates. The resulting radial density gradient gives rise to partial pressure support for fluid in the inner disk and causes the rotation profile to deviate from Keplerian, an issue that we return to in §5.4. Figs. 2a & b show plots of Σ_0 and $\varpi \Omega$, respectively, at various times for simulation 3D9a. It is evident that as the inner region of the disk is depleted of mass, the velocity profile becomes increasingly sub-Keplerian. Both effects can be attributed to radiation of angular momentum away from the inner disk which drives accretion onto the star.

Fig. 1b shows a radius-time image of the radial velocity, and it is clear that there is radial infall in the inner region of the disk, which occurs during the same time as depletion of the inner

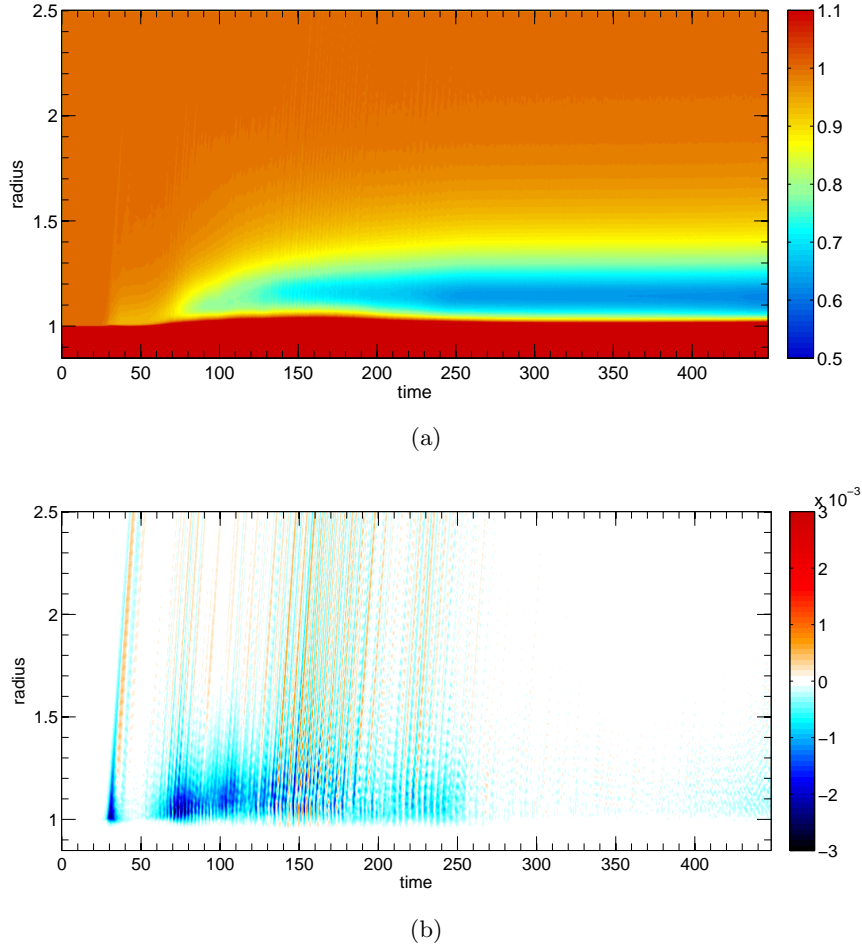


Fig. 1.— Panels a & b show radius-time plots of Σ_0 and $\langle v_\omega \rangle$, respectively for simulation 3D9a.

disk in Fig. 1a. The striations in Fig. 1b correspond to density waves that emanate away from the boundary layer, and their “slant” indicates that by causality they are indeed emitted from the vicinity of the BL.

It is evident from Fig. 1b that after a period of vigorous infall, the radial velocity and hence the accretion rate in the inner disk drops off around $t \sim 250$. This can be attributed to a reduction in the amplitude of waves emitted from the BL, so the rate of angular momentum transport is diminished. Moreover, the pattern speed drops significantly during this period, and it is possible for trapped shocks to develop between the BL and an evanescent region in the disk (Belyaev et al. 2012). The reason for this shift in behavior seems to be related to the angular momentum budget of the inner disk, and we postpone a more detailed discussion of this issue until §5, where we investigate angular momentum transport in depth.

Finally, we comment on a result of Belyaev et al. (2012), where they found the width of the

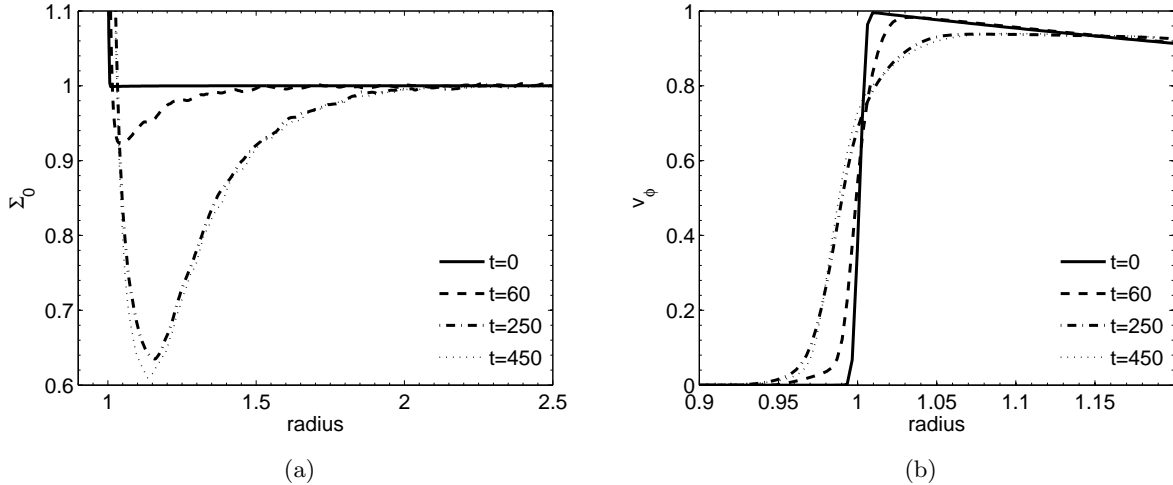


Fig. 2.— Panels a & b show Σ_0 and $\varpi\Omega$ vs. time, respectively, for simulation 3D9a.

BL to extend across 6 – 7 scale heights in the 2D hydro case. Defining the BL as the region in which

$$0.1 < \langle v_\phi(\varpi) \rangle / v_K(\varpi) < 0.9, \quad (29)$$

we find general agreement with the 2D results of Belyaev et al. (2012) in our 3D simulations.

Fig. 3 shows the width of the BL (in scale heights (equation[36])) as a function of time for both our 3D unstratified simulations that span the full 2π in azimuthal angle (solid lines) and the 3D stratified simulations (dashed lines). The color denotes Mach number with black corresponding to $M = 9$ and red corresponding to $M = 6$.

We point out that there is a sizeable degree of scatter among the simulations in Fig. 3, but that the mean is around 6 scale heights, which is consistent with 2D simulations. One possible reason for the larger amount of scatter in the 3D case is that the 2D simulations were run for a longer time, and the measurement of BL width was performed at a later time in the runs. Thus, the BL in our 3D simulations may still be settling down to its steady state width.

We now turn to the modal structure of the BL, since it is ultimately waves which transport angular momentum in our simulations. Thus, understanding the dispersion relation of the BL is instrumental to understanding angular momentum transport by these waves.

4. Boundary Layer Modes

We find in our simulations that the shear in the boundary layer can generate three distinct types of $k_z = 0$ acoustic modes. These three types of modes are directly related to the upper,

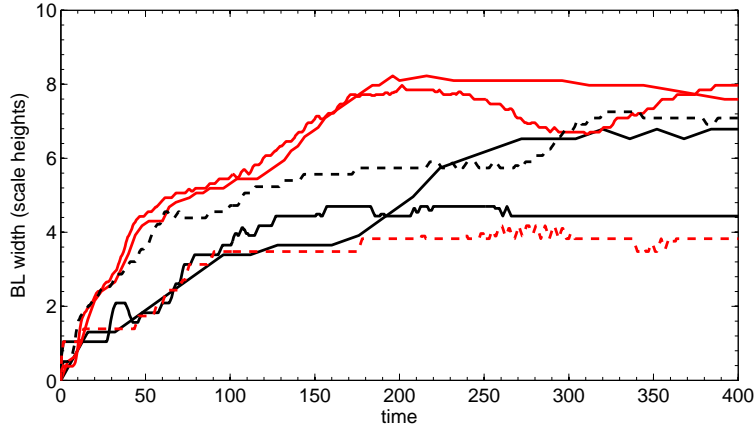


Fig. 3.— Width of the BL in scale heights as a function of time. The dashed curves correspond to 3D stratified simulations and the solid lines to 3D unstratified simulations spanning the full 2π in azimuthal angle. The color differentiates Mach number with $M = 9$ in black and $M = 6$ in red.

lower, and middle branches discussed in Belyaev & Rafikov (2012) for a 2D plane parallel vortex sheet in the supersonic regime. However, the dispersion relation for these modes is modified in a simple way by the radial stratification in the star and the Coriolis force in the disk. To begin our discussion, we first review the dispersion relation of the 2D plane parallel vortex sheet.

4.1. Plane Parallel Vortex Sheet

In the absence of stratification or Coriolis force, the dispersion relation for a 2D vortex sheet (with x and y coordinates locally representing ϖ and ϕ coordinates in the BL) with velocity profile

$$V_y(x) = \begin{cases} V, & x > 0 \\ 0, & x < 0, \end{cases} \quad (30)$$

sound speed s_+ for $x > 0$, and sound speed s_- for $x < 0$ in the limit $V \gg s$ is given by (Belyaev & Rafikov 2012)

$$\omega/|k_y| \approx \begin{cases} V - s_+, & \text{Upper branch} \\ V \left(\frac{s_+}{s_+ + s_-} \right), & \text{Middle branch} \\ s_-, & \text{Lower branch.} \end{cases} \quad (31)$$

Note that by pressure balance $\rho_+/\rho_- = (s_-/s_+)^2$, assuming γ is everywhere constant. All three branches in equation (31) are sonic in nature, with outgoing sound waves emitted from the vortex sheet at $x = 0$.

The upper and lower branches have the property that the sound waves emitted from the vortex sheet in the half-planes $x > 0$ and $x < 0$, respectively, propagate nearly parallel to the vortex sheet.

In other words, $|k_y/k_x| \gg 1$ for the upper and lower branches in the half-planes $x > 0$ and $x < 0$ respectively. The middle branch has the property that $|k_y/k_x|$ is the same on both sides of the vortex sheet. Thus, the wavefronts form the same angle with the vortex sheet in both the $x > 0$ and $x < 0$ half-planes. This is true even if the densities are different in the two half-planes. These sets of properties for the isothermal vortex sheet are instrumental in determining how the dispersion relations for each of the three wave branches are modified in going to the disk-star system.

Panels a-c of Fig. 4 are schematics, which depict the geometry of the wavefronts for δv_x , the perturbed velocity perpendicular to the vortex sheet, for each of the three branches. The arrows show the direction of the flow, and the solid vertical line is the vortex sheet at $x = 0$. At the vortex sheet, δv_x undergoes both a change in amplitude and a change in sign (see equation (36) of Belyaev & Rafikov (2012)). Thus, the wavefronts of δv_x appear shifted in phase by π across the vortex sheet.

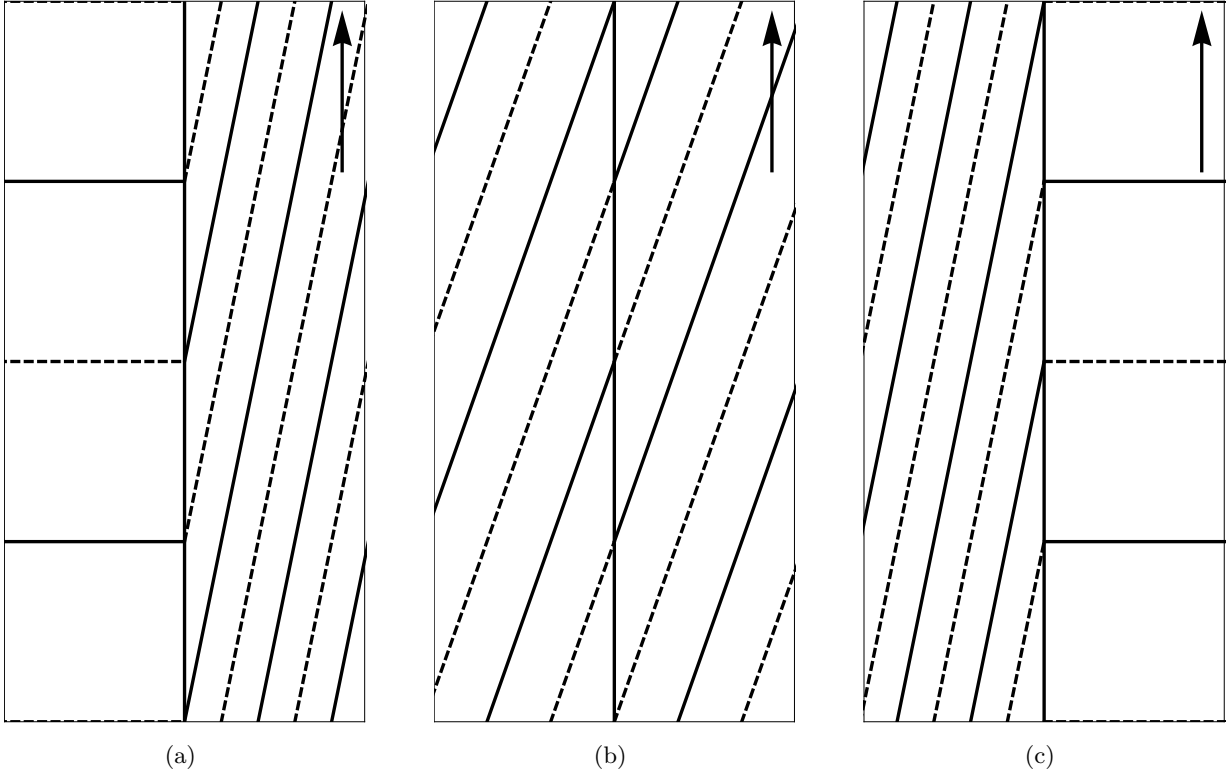


Fig. 4.— a) Wavefronts of δv_x for the lower wave for $M = 6$. The arrow depicts the direction of the flow in the $x > 0$ half-plane. The vortex sheet itself is depicted by the solid vertical line and is located at $x = 0$. The solid lines depict wave crests, and the dashed lines depict troughs. Notice that the perturbation to δv_x undergoes a change in sign (phase shift by π) at the vortex sheet. Panels b) and c) are the same as a), but for the middle and upper waves respectively.

4.2. Dispersion Relations for the Isothermal Boundary Layer

We now discuss how the dispersion relations for each of the wave branches in the isothermal vortex sheet given by equation (31) are modified in going to the disk-star system. As a result, we find accurate, though, heuristic dispersion relations for the generalization of these modes to the isothermal boundary layer studied in our simulations.

4.2.1. Upper Branch

As discussed in §4.1, the upper branch for the vortex sheet is characterized by a sound wave with phase speed $V - s_+$ in the half-plane $x > 0$, which propagates nearly parallel to the vortex sheet, i.e. $|k_y/k_x| \gg 1$.

In order to generalize this to the disk-star system, we postulate that in the disk-star system there is a branch characterized by a density wave in the disk that has $|k_\phi/k_\varpi| \gg 1$ at $\varpi = \varpi_*$. Here, and throughout the paper, we shall define $k_\phi \equiv m/\varpi$, where m is the azimuthal pattern number.

Since, $|k_\phi/k_\varpi| \gg 1$ in the disk near the BL, the wave fronts are very loosely wound, and we cannot apply the classical dispersion relation for a fluid disk in the tight-winding limit (Goldreich & Tremaine 1978). However, it is straightforward to derive an approximate dispersion relation for a loosely wound density wave, if we additionally assume $m \gg 1$ (Appendix A). The result is

$$(\Omega - \Omega_P)^2 = \left(\frac{s}{\varpi}\right)^2 + \left(\frac{\kappa}{m}\right)^2. \quad (32)$$

Equation (32) generally has two solutions with one having $\Omega_P > \Omega$ and the other $\Omega_P < \Omega$. For the isothermal vortex sheet, it turned out that the physical solutions, corresponding to outgoing waves have a phase velocity $\omega/k < V$ (Belyaev & Rafikov 2012). By analogy, we take the solution to equation (32) having $\Omega_P < \Omega$ to be the physical one. In that case, taking $\varpi = \varpi_*$, $V = \varpi_*\Omega(\varpi_*)$, and making the associations $\omega = m\Omega_P$, and $k_y = m/\varpi_*$, we see that equation (32) is analogous to equation (31) for the upper branch of the vortex sheet, except for the additional term containing the epicyclic frequency, which is due to the Coriolis force.

We can generalize equation (32) to arbitrary values of k_ϖ by writing

$$m^2(\Omega - \Omega_P)^2 = s^2(k_\phi^2 + k_\varpi^2) + \kappa^2. \quad (33)$$

This approximate dispersion relation reduces to the one for tightly-wound waves in the limit $|k_\varpi/k_\phi| \gg 1$ (Goldreich & Tremaine 1978) and to equation (32) in the limit $|k_\phi/k_\varpi| \gg 1$. Thus, it is accurate in both the tight-winding and loose-winding limits. The essential modification to the tightly-wound dispersion relation is the replacement of the radial wavenumber with the total wavenumber inside the braces in equation (33) i.e. $k_\varpi^2 \rightarrow k_\varpi^2 + k_\phi^2$.

An important feature of equation (33) is that it predicts an evanescent region in the disk directly adjacent to the BL. This can be deduced by noting that the left hand side of equation (33) vanishes when $\Omega = \Omega_P$, implying that k_ϖ is imaginary at the corotation radius.

Table 2 compares the value of Ω_P observed in simulations when the upper wave is present to that predicted by the dispersion relation (32). For simplicity, we set $\varpi = \varpi_\star$ and use the Keplerian values of Ω and κ when calculating the predicted values from equation (32), i.e. all variables are evaluated just outside the BL. Nevertheless, the agreement between the analytical predictions and the simulations is good to the level of several percent for both 2D and 3D simulations and irrespective of stratification. However, some of our theoretical estimates tend to be slightly high, especially at late times ($t \gtrsim 60$ orbits) when the boundary layer has thickened substantially. One possible cause for the slight deviation between the measured and analytically predicted pattern speeds is that the boundary layer is not infinitesimally thin, but we have assumed so in evaluating the dispersion relation at $\varpi = \varpi_\star$.

| label | time | m | Ω_P measured | Ω_P predicted |
|-------|------|--------------|---------------------|----------------------|
| 2D6a | 20 | ≈ 40 | .84 | .831 |
| 2D6b | 20 | ≈ 40 | .835 | .831 |
| 2D6c | 20 | ≈ 40 | .835 | .831 |
| 3D6c | 120 | 9 | .77 | .80 |
| 3D9a | 100 | 10 | .83 | .850 |
| 3D9d | 60 | 12 | .85 | .861 |
| 2D9a | 30 | ≈ 29 | .87 | .884 |
| 2D9a | 280 | 11 | .815 | .856 |
| 2D9b | 30 | ≈ 24 | .87 | .881 |
| 2D9c | 30 | ≈ 32 | .88 | .885 |

Table 2: Comparison between the analytical value of Ω_P and the value measured in simulations for the upper branch. The columns are from left to right: simulation label, time since the start of the simulation, m , pattern speed measured from the simulation, pattern speed predicted from equation (32).

Table 2 shows that the behavior of the phase speed of the upper mode is in reasonable agreement with the simple vortex sheet prediction (31). Indeed, the latter would result in $\Omega_P = \omega/(k_y \varpi_\star) \approx 0.83$ and 0.89 for $M = 6$ and 9 correspondingly. This agrees with the trend seen in our simulations, where a higher value of M results in a somewhat larger value of Ω_P . Also, the magnitude of Ω_P is close to $\Omega_K(\varpi_\star)$, in accord with equation (31) for high Mach number.

4.2.2. Lower Branch

For the case of the isothermal vortex sheet (§4.1), the lower branch is characterized by a sound wave which propagates nearly parallel to the vortex sheet in the half-plane $x < 0$ with phase velocity s_- . We now discuss the modifications that need to be made to this dispersion relation in order to apply it to the disk-star system.

We begin by postulating that the lower branch in the disk-star system is characterized by a sound wave which propagates azimuthally in the star. One immediate difference as compared to the isothermal vortex sheet case is that the star is stratified, so the phase velocity of the lower branch is not simply s , but is modified by the effects of gravity and stratification.

In a non-moving, plane-parallel atmosphere stratified in the x -direction with constant sound speed, s , and gravity, g , the dispersion relation for gravito-sonic waves (p and g modes) is given by e.g. Vallis (2006) as

$$\omega^2 = \frac{s^2 l^2}{2} \left[1 \pm \left(1 - \frac{4(\gamma - 1)k_y^2}{\gamma^2 h_s^2 l^4} \right) \right] \quad (34)$$

$$l^2 \equiv k_x^2 + k_y^2 + 1/4h_s^2 \quad (35)$$

$$h_s \equiv s^2/\gamma g, \quad (36)$$

where h_s is the pressure scale height. Note that the dispersion relation (34) applies to *all wavelengths*, not just to those that are short compared to the scale height of the atmosphere.

The upper sign inside the braces on the right hand side of equation (34) corresponds to p-modes and the lower sign to g-modes. An isothermal equation of state ($\gamma = 1$) is neutrally buoyant, so g-modes have $\omega = 0$, and we will not consider them further. On the other hand, the dispersion relation for p-modes with $\gamma = 1$ reduces to

$$\omega^2 = s^2 \left(k_x^2 + k_y^2 + \frac{1}{4h_s^2} \right). \quad (37)$$

Note that the effect of gravity and stratification enters into the dispersion relation through the $1/4h_s^2$ term, and in the limit $h_s \rightarrow \infty$ we recover the dispersion relation for a sound wave in a uniform medium. However, since we typically find $\lambda \gtrsim h_s$ in our simulations for the dominant modes, the stratification term in equation (37) is very important for comparing with simulations.

We can use equation (37) to derive a dispersion relation for the generalization of the lower branch to the disk-star system. We start by setting $k_y = m/\varpi$, and by analogy with the vortex sheet, we assume that $|k_y/k_x| \gg 1$ inside the star. Making again the association, $\omega = m\Omega_P$, we

have

$$\Omega_P = s \sqrt{\left(\frac{1}{\varpi_0}\right)^2 + \left(\frac{1}{2mh_s(\varpi_0)}\right)^2} \quad (38)$$

$$= \Omega(\varpi_\star) \frac{\varpi_\star}{\varpi_0} \sqrt{M^{-2} + \left(\frac{M}{2m} \frac{\varpi_\star}{\varpi_0}\right)^2}. \quad (39)$$

Since Ω_P must be independent of radius, we have chosen an “effective radius”, $\varpi_0 \lesssim \varpi_\star$, to use in the expression on the right-hand side of equation (38). Although the choice of an effective radius may seem like an “ad-hoc” prescription, we provide theoretical justification for it in Appendix B. It is further justified by the agreement between the value of $\Omega_P(m, M)$ measured in simulations and that given by equation (38).

Figure 5 shows a plot of Ω_P vs. m from our simulations when the lower wave is observed. It is evident that the agreement between equation (38) and the data is quite good over a wide range of values for m and Ω_P . Moreover, the 2D simulations (circles), 3D unstratified simulations (squares), and 3D stratified simulations (triangles) lie on the same curve for both $M = 6$ and $M = 9$, implying that the behavior is fundamentally the same in both 2D and 3D and with or without stratification.

It is of note that the lower mode in the BL has phase speed considerably higher than $\Omega_P = M^{-1}\Omega(\varpi_\star)$ predicted by the simple vortex sheet model, see equation (31). This is because the results presented in §4.1 were obtained assuming an *unstratified* star, in which case $h_s \rightarrow \infty$ and our BL dispersion relation (38) would reduce to its vortex sheet analog. However, in an isothermally stratified star, the density gradient strongly modifies the dispersion relation, as evidenced by the second term in equation (39), and makes Ω_P not only a function of M but also of m , the azimuthal wavenumber.

4.2.3. Middle Branch

For the isothermal vortex sheet with a constant sound speed everywhere throughout the domain ($s_+ = s_-$), the phase velocity of the middle branch is simply $V/2$ (§4.1). Moreover, the wavefronts make the same angle with respect to the vortex sheet both above and below it, which is true even for the case of non-equal densities above and below the vortex sheet (Belyaev & Rafikov 2012). This last fact can be expressed mathematically as $k_{x,+}/k_y = k_{x,-}/k_y$, where the plus and minus signs denote the value of k_x in the $x > 0$ and $x < 0$ half-planes, respectively.

We now postulate that for the disk-star system the wavefronts in the star and in the disk form the same angle with respect to the azimuth across the boundary layer. Using equations (33) and

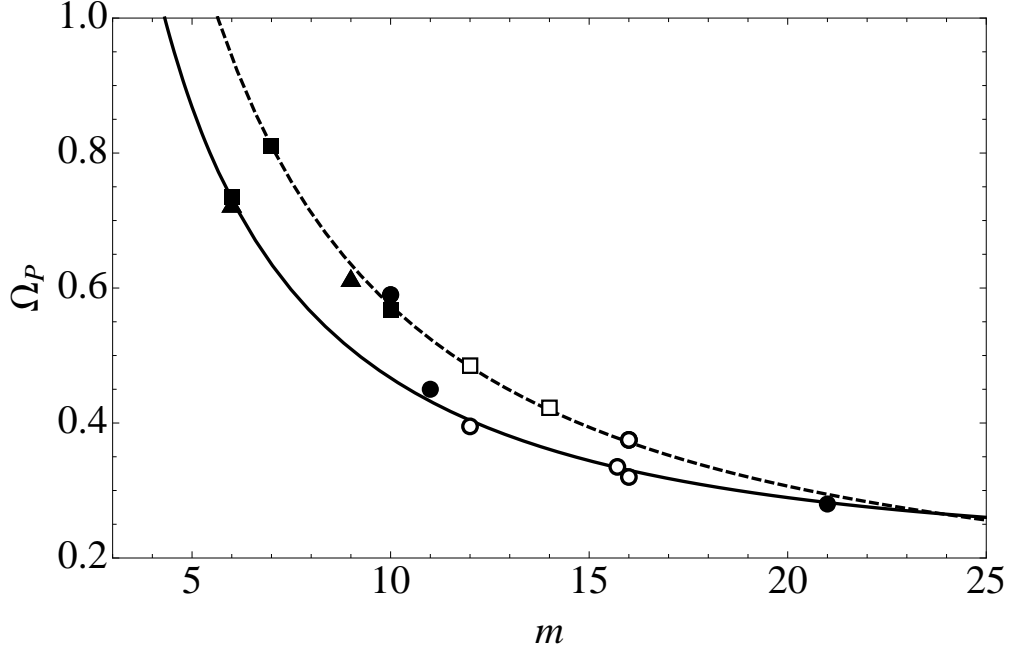


Fig. 5.— Comparison between the analytical dispersion relation, $\Omega_P(m, M)$, and simulation results for the lower branch. The solid line is the analytical prediction from equation (38) for $M = 6$ using an effective radius of $\varpi_0 = .84$, and the dashed line is for $M = 9$ using $\varpi_0 = .90$. The points show values of Ω_P and m measured from simulations when the lower branch is dominant. The circles represent 2D simulations, the squares 3D unstratified simulations, and the triangles 3D stratified simulations. Filled points represent simulations spanning the full 2π in azimuthal angle, and open points represent simulations for a wedge which spans an azimuthal angle $< 2\pi$. There is a solid triangle and a solid square that have merged near the solid curve at $M = 6$.

(37), we can write

$$\left(\frac{k_{\varpi, \text{disk}}}{k_\phi}\right)^2 = \frac{(\omega - m\Omega)^2 + \kappa^2}{(sk_\phi)^2} - 1 \quad (40)$$

$$\left(\frac{k_{\varpi, \text{star}}}{k_\phi}\right)^2 = \frac{\omega^2}{(sk_\phi)^2} - \frac{1}{(2h_s k_\phi)^2} - 1 \quad (41)$$

Setting equations (40) and (41) equal to each other at $\varpi = \varpi_*$ (the condition that the wavefronts in the disk and star form the same angle with respect to the azimuth across the BL), the dispersion relation for the middle branch is

$$\Omega_P = \frac{\Omega(\varpi_*)}{2} \left[1 + \frac{1}{m^2 \Omega^2(\varpi_*)} \left(\kappa^2(\varpi_*) + \frac{s^2}{4h_{s,*}^2} \right) \right]. \quad (42)$$

Table 3 lists the pattern speeds and m -numbers measured in simulations when the middle branch is clearly dominant and compares the pattern speed to that predicted by equation (42). For

simplicity, we again assume a Keplerian profile for κ and Ω when computing the predicted pattern speed. The agreement between the predicted and measured values is at the several percent level. Also, Ω_P is close to $\Omega(\varpi_\star)/2$, in agreement with the vortex sheet model, see equation (31). The discrepancy between the measured and analytically-predicted pattern speeds could arise because the condition $k_{\varpi,+}/k_\phi = k_{\varpi,-}/k_\phi$ is not exactly satisfied for the disk-star system as it is for the isothermal vortex sheet. Nevertheless, we find that equation (42) provides a good approximation to the pattern speed observed in our simulations when the middle branch is dominant. We also note that we have fewer measurements for the middle branch as compared to the upper and lower branches, because the middle branch is a transient phenomenon observed only during the linear growth regime of the sonic instabilities, if at all.

| label | time | m | Ω_P measured | Ω_P predicted |
|-------|------|--------------|---------------------|----------------------|
| 3D6a | 10 | ≈ 42 | .52 | .502 |
| 3D6d | 10 | ≈ 36 | .515 | .503 |
| 3D6c | 10 | ≈ 44 | .52 | .502 |
| 3D9e | 20 | ≈ 28 | .57 | .515 |

Table 3: Comparison of the analytically predicted value of Ω_P , and the value measured from simulations for the middle branch. The columns of the table are from left to right: simulation label, time since the start of the simulation, m , pattern speed measured from the simulation, pattern speed predicted by equation (42).

4.3. Spatial Morphology of the Upper, Middle, and Lower Branches

We have identified three branches in our simulations that are the generalizations of the upper, middle, and lower branches of the 2D isothermal vortex sheet. We now discuss the structural morphology of each of these branches.

Fig. 6 shows snapshots of $\varpi\sqrt{\Sigma}\langle v_\varpi \rangle_z$ vertically-averaged in the z -direction for each of the three wave-branches from 3D unstratified simulations. The quantity $\varpi\sqrt{\Sigma}\langle v_\varpi \rangle_z$ is approximately constant throughout the star and disk, so it is especially useful for visualizing the radiation pattern. This is because waves conserve energy and angular momentum current, which are both of order $\varpi^2\Sigma\delta v^2$, where δv is the magnitude of the velocity perturbation. The dashed and dotted vertical lines in Fig. 6 depict the edges of evanescent regions and corotation radii respectively. Notice that there are always two corotation radii: one inside the boundary layer at $\varpi \approx 1$, and one inside the evanescent region within the disk. In principle, there is also an evanescent region around the corotation radius inside the BL, but this region is narrow, due to the steep radial gradient of angular velocity within the BL.

The sharp features seen in this Figure (especially in panel b) are the shocks into which the propagating acoustic modes evolve as a result of their nonlinearity. Even though the nonlinearity

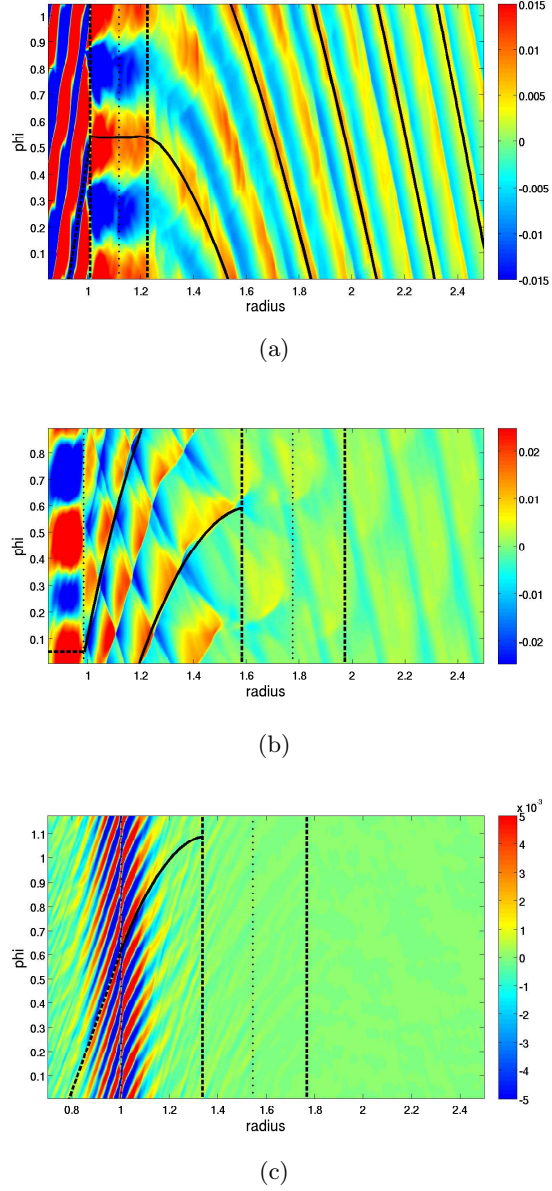


Fig. 6.— Panels a, b, c show snapshots of $\varpi \sqrt{\Sigma} \langle v_{\varpi} \rangle_z$, when the upper, lower, and middle branches are dominant. Panel a corresponds to simulation 3D9d at $t = 65$, b to simulation 3D9e at $t = 320$, panel c to simulation 3D6a at $t = 10$. Dashed vertical lines depict the boundaries of evanescent regions and dotted vertical lines depict corotation radii.

is relatively mild, with $v_{\varpi} \sim 0.1s$, implying density jump of $\sim 10\%$ across the shock fronts in this particular simulation (see also Fig. 10), the waves propagating into the disk break and become weak shocks. In our simulations we typically find this to occur not too far from the BL, at separations of $(0.2 - 1)\varpi_{\star}$ away from their launching point.

The solid and dashed curves in Figure 6 trace the shape of shock fronts or wave fronts if the wave has not shocked. The formula for the shape of a front is simply

$$\frac{d\phi}{d\varpi} = \pm \frac{k_{\varpi}}{k_{\phi}}, \quad (43)$$

where k_{ϖ} is given by formula (33) inside the disk or (37) inside the star. The sign on the right hand side of equation (43) determines whether the wave front is angled up or down, assuming we take k_{ϖ} and k_{ϕ} to be positive. We see from Figure 6 that the analytic curves for the shock fronts are in excellent agreement with snapshots from the simulations, which is due to the fact that waves are only weakly nonlinear.

For the upper branch, which has high Ω_P close to unity, the evanescent region extends all the way down to the boundary layer, so density waves emitted from the BL that propagate into the disk have a pattern speed that is faster than the angular speed of the disk material and wind up with increasing radius. For the lower and middle branches, however, the evanescent region in the disk is well-separated from the boundary layer, so density waves emitted from the BL have a slower pattern speed than the angular speed of the disk material. These density waves unwind as they travel towards the forbidden region, partially reflecting off it, with very little transmission (see §5.2 for a lower bound on the reflection coefficient measured from simulations).

As a result of this reflection, a standing shock pattern can be set up in the disk between the BL and the forbidden region (Fig. 6b) if a resonance criterion is satisfied. This criterion states that in order to achieve standing shocks, the total azimuthal angle subtended by a shock in traveling from the BL to the forbidden region and back must be an integer multiple of the angle subtended by one wavelength of the mode. Mathematically, this criterion is

$$\frac{2\pi p}{m} = 2\Delta\phi_{\text{shock}} \quad (44)$$

$$\Delta\phi_{\text{shock}} = \int_{\varpi_{\text{BL}}}^{\varpi_0} d\varpi \frac{d\phi}{d\varpi}, \quad (45)$$

see Belyaev et al. (2012) for more details. Here, ϖ_0 is the inner edge of the forbidden region in the disk, $\varpi_{\text{BL}} \approx 1$, and $d\phi/d\varpi$ is given by equation (43). The integer $p \geq 1$ gives the number of shock crossings for a shock traveling from the BL to the forbidden region or vice versa, counting the reflection point at the edge of the evanescent region as a shock crossing. For instance, solving equation (44) for the $m = 14$ mode depicted in Fig. 6b we find $p = 6.03$. Thus, p is very close to an integer, which allows the standing shock pattern to form, and it is evident that each outgoing and incoming shock undergoes six shock crossings (counting the point of reflection).

Although p does not necessarily need to be an integer, it is likely that modes with an azimuthal wavenumber, m , that is close to an integer value of p are reinforced relative to modes with a similar value of m , but for which p is not close to an integer by the resonance condition.

4.4. Modes with $k_z \neq 0$

The upper, lower, and middle branch modes are all two-dimensional in the $\varpi - \phi$ plane in the sense that they do not require the z -dimension to operate. In principle, there are also Kelvin-Helmholtz (KH) modes for vertical wavenumbers $k_z/k_\phi \gtrsim M$ (Belyaev & Rafikov 2012).

To determine the relative importance of the $k_z \neq 0$ vs. the $k_z = 0$ modes, we compute the power spectrum from the unstratified simulations along the z -dimension. We work in the variable $\delta\rho/\sqrt{\Sigma_0}$, which by the definition of $\delta\rho$ (equation [12]) sums to zero when integrated over the entire simulation domain. This is a natural variable to use, since one expects the time-averaged value of $|\delta\rho/\sqrt{\Sigma_0}|$ to be roughly constant for a wave across the entire simulation domain up to factors related to the geometry and rotation profile.

To obtain the power spectrum, we first perform a discrete Fourier transform in the z -direction. In order to carry out summations, we let $\delta\rho/\sqrt{\Sigma_0}$ be a function of the grid points (l, m, n) in the (ϖ, ϕ, z) , directions respectively. The Fourier transform in the z -direction then becomes

$$\mathcal{F}_n(l, m) \equiv \frac{1}{\sqrt{N_z}} \sum_{n=0}^{N_z-1} e^{-i2\pi n z/N_z} \frac{\delta\rho(l, m, n)}{\sqrt{\Sigma_0(l)}}, \quad (46)$$

where N_z is the number of cells in the z -dimension. The power spectrum is then defined as

$$P_n \equiv \frac{1}{N_\varpi N_\phi N_z} \sum_{l=0}^{N_\varpi-1} \sum_{m=0}^{N_\phi-1} (\mathcal{F}_n(l, m))^2. \quad (47)$$

We note that by Parseval's theorem,

$$\sum_{n=0}^{N_z-1} P_n = \frac{1}{N_\varpi N_\phi N_z} \sum_{n=0}^{N_z-1} \sum_{m=0}^{N_\phi-1} \sum_{l=0}^{N_\varpi-1} \left(\frac{\delta\rho(l, m, n)}{\sqrt{\Sigma_0(l)}} \right)^2. \quad (48)$$

Fig. 7 shows power spectra computed from the simulations. Plotted is $\log_{10}(P_n/\sum_n P_n)$ vs. k_z , where $k_z \equiv 2\pi n/\Delta z$, and Δz is the width of the simulation domain in the z -direction. The black lines are from simulation 3D9e, and the red lines are from simulation 3D9f which has the same parameters but twice the z -resolution. The solid lines correspond to a time when the upper mode is dominant, and the dashed lines to a time when the lower mode is dominant. From the figure, it is clear that the $n = 0$ mode has at least several orders of magnitude more power than all of the $n > 0$ modes combined. Note that we only plot the modes from $n = 0$ to $n = N_z/2$, where $N_z/2 = 16$ for simulation 3D9e. This is because modes having $n = N_z/2 + 1$ to $N_z - 1$ (if N_z is divisible by 2) are just the complex conjugates of modes having $n = N_z/2 - 1$ to $n = 1$, for a real signal with no imaginary component, such as ours. Simulation 3D9f has $N_z/2 = 32$, but we only show the modes up to $n = 16$, since there are no interesting features past $n > 16$, and the power spectrum simply continues to decay with increasing n .

It is clear from Fig. 7 that there is more power in the $k_z \neq 0$ modes relative to the $k_z = 0$ mode for the higher resolution simulation as compared to the lower resolution simulation. Thus, it is possible that our simulations are not fully converged in the z -direction. Nevertheless, the fact that the power in the $k_z \neq 0$ modes is still several orders of magnitude less than the power in the $k_z = 0$ mode even for the higher resolution simulation suggests that the $k_z = 0$ mode is indeed dominant irrespective of the resolution in z .

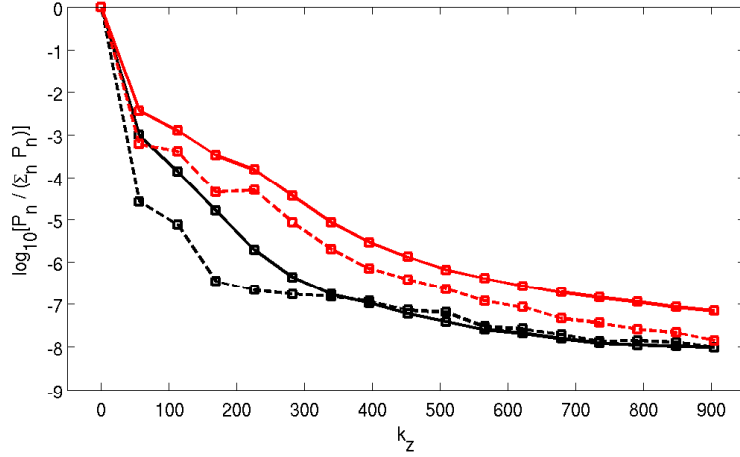


Fig. 7.— The power spectrum, $\log_{10}(P_n / \sum_n P_n)$ as a function of k_z . The solid lines are for the upper mode and the dashed lines for the lower mode. Simulation 3D9e is shown in black and 3D9f in red. Note that simulations 3D9e and 3D9f have the same vertical extent, Δ_z , but a different resolution in the z -direction. When comparing across simulations with different resolutions, one should compare k_z rather than n , since modes with the same value of k_z correspond to the same vertical wavelength, which is not true for modes with the same n if the simulations have different resolutions.

Fig. 8 shows a k_z -time plot of $\log_{10}(P_n)$ for simulations 3D9e and 3D9f. One can see interesting temporal features, such as rapid excitation of both $k_z \neq 0$ modes and $k_z = 0$ modes and their gradual subsequent decay. One possible source for these periodic outbursts are secondary KH instabilities Belyaev et al. (2012). However, in the 3D case, unlike the 2D case, a kink-like inflection point in the azimuthal velocity profile does not form, so this mechanism is not certain. It is also evident in Fig. 8 that the higher resolution simulation (3D9f) has a greater proportion of power in the $k_z \neq 0$ modes, but again the $k_z = 0$ mode is clearly dominant for the duration of the simulation even in the higher resolution case. Thus, one would expect the $k_z = 0$ modes to dominate the angular momentum transport in the system, which we show explicitly in the next section.

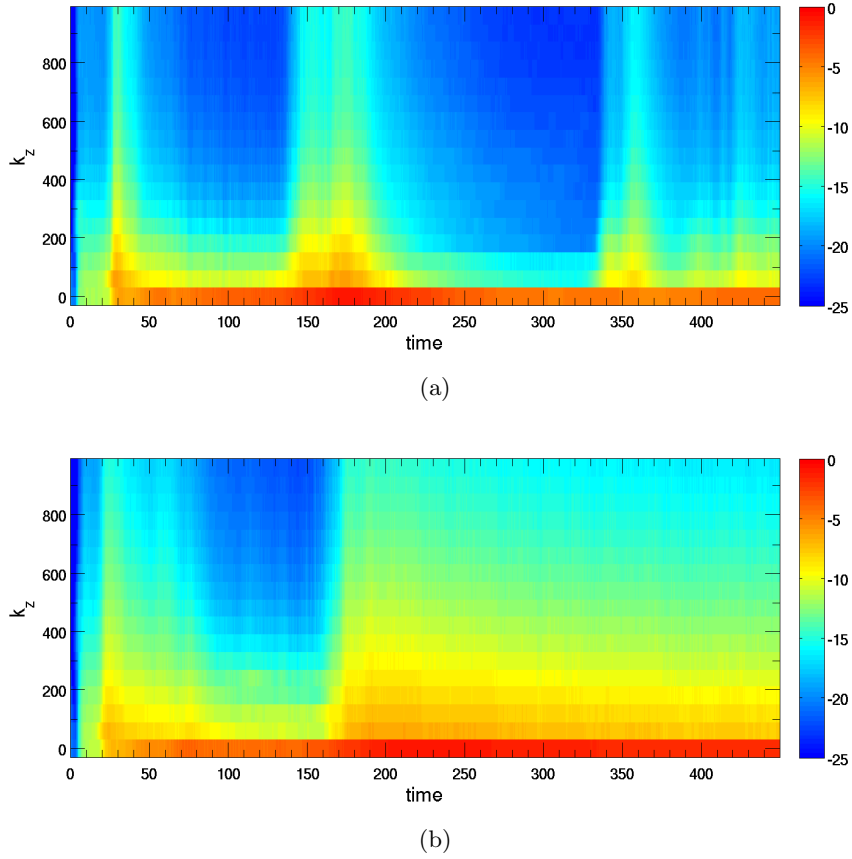


Fig. 8.— a) k_z -time plot of $\log_{10}(P_n)$ for simulation 3D9e. b) k_z -time plot of $\log_{10}(P_n)$ for simulation 3D9f, which has all the same parameters as simulation 3D9e, except that the z -resolution has been doubled. We again point out that comparing across simulations with different resolutions, one should compare k_z rather than n , since modes with the same value of k_z correspond to the same vertical wavelength.

5. Angular Momentum Transport

Here we discuss angular momentum transport due to the upper and lower wave branches. We find good agreement between theory and simulation and conclude that the upper branch is more efficient at transporting angular momentum. We do not consider the middle branch here, since it is dominant only for short periods of time while the instabilities are still growing.

As we shall soon demonstrate, angular momentum transport in our simulations is dominated not by turbulent stresses, but rather by acoustic radiation of angular momentum away from the boundary layer both into the star and into the disk. Moreover, the $k_z = 0$ modes dominate the angular momentum transport, as hinted at in §4.4, which allows us to use the theory of density waves in thin disks to calculate the rate of angular momentum transport (e.g. Appendix J of Binney

& Tremaine (2008)).

The angular momentum current through radius ϖ is given by equation (19). By analogy with equation (20), it can be decomposed into a stress term and an advective term.

$$C_S(\varpi) \equiv 2\pi\varpi F_S \quad (49)$$

$$C_A(\varpi) \equiv 2\pi\varpi F_A. \quad (50)$$

Waves transport angular momentum exclusively through stresses, and we can use equations (49) and (22) to calculate C_S . Inside the star, C_S for a given mode with azimuthal wavelength m is given in terms of the amplitude of the density perturbation $\delta\Sigma_m(\varpi)$, as

$$C_{S,m}(\varpi) = \pm \left(\frac{k_\varpi \varpi}{m} \right) \frac{\pi s^4 \Sigma_0}{\Omega_P^2} \left(\frac{\delta\Sigma_m}{\Sigma_0} \right)^2. \quad (51)$$

Here we have used the relations in Appendix B to express $\delta v_{\phi,m}$ and $\delta v_{\varpi,m}$ in terms of $\delta\Sigma_m$. The total angular momentum current due to waves is the sum over all modes for both incoming and outgoing waves and is given by

$$C_S(\varpi) = \sum_m C_{S,m}(\varpi). \quad (52)$$

We next assume that all waves propagate outwards from the BL, and that $k_\varpi \varpi / m$ is relatively insensitive to m near the dominant m value, which we denote as \bar{m} . This pair of assumptions will be verified later by comparison with simulation results. However, it fixes the sign in equation (51) and allows us to use Parseval's theorem (Belyaev et al. 2012) to write the total stress due to waves in the star as

$$C_S(\varpi) = - \left(\frac{k_\varpi(\bar{m})\varpi}{\bar{m}} \right) \frac{s^4 \Sigma_0}{\Omega_P^2} \int_0^{2\pi} d\phi \left(\frac{\delta\Sigma}{\Sigma_0} \right)^2. \quad (53)$$

The analog to equation (53) for the angular momentum current due to density waves in the disk is (Binney & Tremaine 2008; Belyaev et al. 2012)

$$C_S(\varpi) = \left(\frac{k_\varpi(\bar{m})\varpi}{\bar{m}} \right) \frac{s^4 \Sigma_0}{(\kappa/m)^2 - (\Omega - \Omega_P)^2} \int_0^{2\pi} d\phi \left(\frac{\delta\Sigma}{\Sigma_0} \right)^2, \quad (54)$$

where we have again used Parseval's theorem and assumed that all waves propagate away from the BL.

Waves propagating into the disk shock, resulting in $\partial C_S / \partial \varpi \neq 0$ due to dissipation of the wave with increasing distance away from the BL. The shock-related change in angular momentum current carried by the wave as a function of radius in the disk is given by (Larson 1990; Belyaev et al. 2012)

$$\frac{\partial C_S}{\partial \varpi} = -m\varpi \Sigma_0 \frac{dE}{dm}. \quad (55)$$

Here, dE/dm is the energy converted into heat per unit mass of fluid crossing the shock, which comes at the expense of the energy contained in the shock and causes it to damp. For the isothermal case, the expression of Larson (1990) for dE/dm is

$$\frac{dE}{dm} = \frac{s^2}{6} \frac{\epsilon^3}{(1 + \epsilon)^2} \quad (56)$$

in the limit $\epsilon \ll 1$, where $\epsilon \equiv \Delta\Sigma/\Sigma$ is the jump in density across the shock divided by the preshock density.

It is also possible to derive an expression for dE/dm which is valid for arbitrary values of ϵ in the isothermal limit $\gamma \rightarrow 1$ (Appendix C)

$$\frac{dE}{dm} = s^2 \frac{\epsilon(2 + \epsilon) - 2(1 + \epsilon) \ln(1 + \epsilon)}{2(1 + \epsilon)}. \quad (57)$$

This converges to Larson’s result (equation [56]) to leading (third) order in ϵ .

In contrast to waves propagating into the disk, waves propagating away from the BL and into the star do not shock, because their amplitude is proportional to $\rho^{-1/2}$ by conservation of energy and angular momentum. Thus, as waves propagate into the star in our simulations, their amplitude is reduced, nonlinear effects are mitigated, and $\partial C_S / \partial \varpi = 0$. Inside a real star, this reduction in amplitude could not continue indefinitely, and the waves would eventually be absorbed, depositing their energy and angular momentum to the stellar fluid. However this absorption could potentially occur deep inside the star, making the BL appear cooler than if the energy were dissipated locally.

We now apply these results to understand angular momentum transport by the upper and lower acoustic modes, which appear in our simulations most often.

5.1. Upper Branch

5.1.1. Disk

Fig. 9 shows C_S inside the disk for simulation 3D9d at $t \sim 75$, which corresponds to approximately the same time as Fig. 6a, when the upper mode is clearly dominant. The solid black curve shows the measured value of C_S , using equations (22) and (49), and the red curves are the analytically-expected values of C_S , calculated using equation (54) together with the value of $\Delta\Sigma/\Sigma$ across shock fronts measured from simulations. The solid red curve uses the standard WKB expression for k_ϖ (Goldreich & Tremaine 1978), and the dashed red curve uses k_ϖ from equation (33). The standard WKB expression can be obtained from equation (33) by eliminating the k_ϕ term in the brackets. For simplicity, we use the Keplerian values of κ and Ω in equation (54) when calculating the analytically-expected value of C_S (red curves). This is a good approximation, since the rotation profile is very nearly Keplerian in the disk, away from the direct vicinity of the BL.

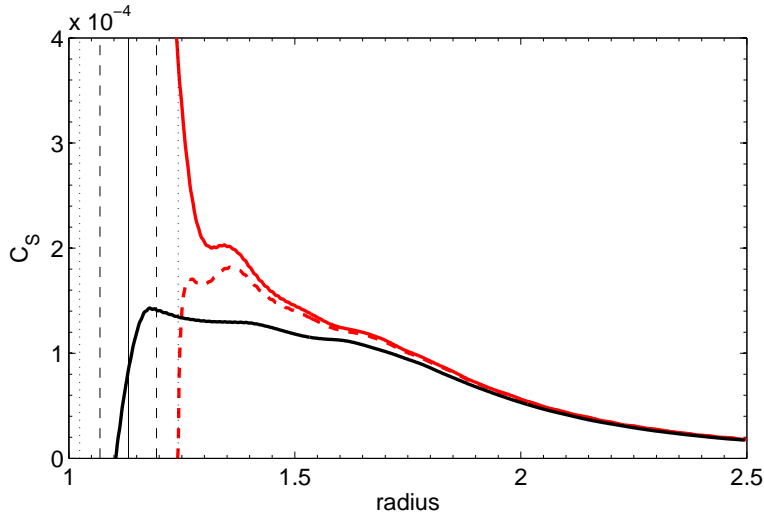


Fig. 9.— Plot of C_S for simulation 3D9d at time $t = 75$ within the disk. See text for details.

Regardless of which form for k_ϖ is employed, equation (54) itself is only valid in the tight-winding approximation. Thus, the red curves converge to the black at large ϖ , but deviate significantly as we approach the evanescent region around corotation, where the upper mode is loosely wound. For the solid red curve, the evanescent region is located between the vertical dashed lines, which correspond to the two Lindblad radii, and for the dashed red curve, the evanescent region is located between the dotted vertical lines. The corotation radius is marked by a solid vertical line. The fact that the red curves converge to the black far away from the evanescent region around corotation is decisive evidence that angular momentum is radiated away from the BL in the form of density waves.

Something else to note is that the black curve in Fig. 9 switches sign close to corotation. This is exactly what would be expected if angular momentum were carried by waves, since the angular momentum density of a wave undergoes a change in sign at the corotation radius (Binney & Tremaine 2008).

We also point out that in Fig. 9 the flux is approximately constant between the edge of the evanescent region and $\varpi \approx 1.7$, but then starts to decrease more rapidly with radius. This reduction in flux is caused by shocking of the wave, which is illustrated in Fig. 10. In this Figure we show the profile of the density perturbation $\Delta\Sigma/\Sigma$ in azimuthal direction, i.e. at fixed ϖ , before (a, at $\varpi = 1.5$) and after (b, at $\varpi = 1.9$) breaking for simulation 3D9d at $t = 75$. It is obvious that in the latter case the wave has shocked, with clear discontinuity in the wave profile, which converges towards the “N-wave” shape (Landau & Lifshitz 1959). Note that the analytically-expected value of C_S (equation [54]), automatically takes into account the dissipation of the wave due to shocking, through the factor of $(\Delta\Sigma)^2$.

We now turn to the reduction of the wave flux with radius after the wave has shocked. Fig. 11

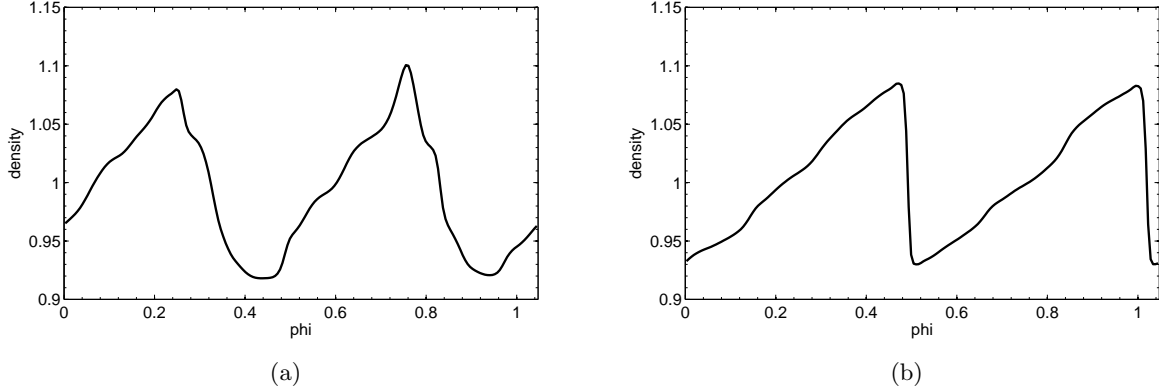


Fig. 10.— Azimuthal profiles of the wave before shocking (panel a) at $\varpi = 1.5$ and after shocking (panel b) at $\varpi = 1.9$.

shows $-\partial C_S/\partial\varpi$ as a function of radius for simulation 3D9d at $t = 75$. The black curve shows the value of $-\partial C_S/\partial\varpi$ computed from the simulation data, where C_S is calculated using equation (49). The red curves are the analytical expectations for $-\partial C_S/\partial\varpi$ due to wave dissipation by shocks calculated using equation (55). The dashed red curve uses the value of dE/dm from equation (56), and the solid red curve uses the value of dE/dm from equation (57).

In measuring $\Delta\Sigma/\Sigma$ in order to calculate dE/dm , we find it necessary to correct for the finite width of the shock in the simulation. This is because the shock in our simulations extends over several cells and is not a true discontinuity. Thus, we extrapolate the shock density profile from a simulation and estimate what the value of $\Delta\Sigma/\Sigma$ would be for a true discontinuity. For our resolution, this correction increases $\Delta\Sigma/\Sigma$ by $\approx 8\%$. Given the stiff dependence of dE/dm on $\Delta\Sigma/\Sigma$ (leading order dependence is $(\Delta\Sigma/\Sigma)^3$, see equation (56)), this correction is necessary to obtain good agreement between theory and simulations.

The agreement between the measured value of $\partial C_S/\partial\varpi$ and the theoretically-predicted one indicates that angular momentum radiated away from the evanescent region into the disk is redistributed by shock dissipation. This dissipation is most vigorous after the wave has completely shocked around $\varpi \approx 1.8$, but the steepest parts of the wave may shock even earlier at $\varpi < 1.8$, so the wave angular momentum starts to be redistributed to the disk fluid even before the entire wave has shocked. Since $\Omega_P > \Omega$ for the upper branch outside the evanescent region in the disk, the wave carries *positive* angular momentum, and dissipation of the wave *spins up* the disk fluid, pushing matter *outward*, see §5.4.

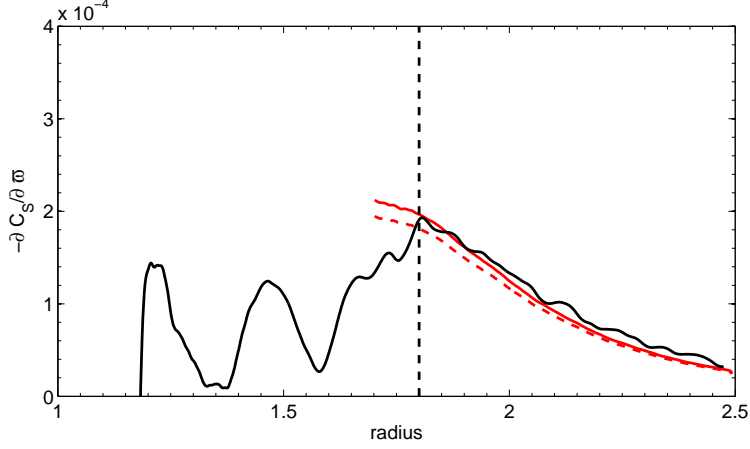


Fig. 11.— Plot of $-\partial C_S/\partial\varpi$ for simulation 3D9d at time $t = 75$. The dashed black line at $\varpi = 1.8$ denotes the radius at which the entire wave has shocked.

5.1.2. Star

Radiation from the BL is emitted not only into the disk, but into the star as well. The amplitude of acoustic waves traveling into the star is proportional to $\rho^{-1/2}$, so they don’t shock in our simulations and propagate out through the inner boundary of the simulation domain.

The inner radial “do nothing” boundary condition is not perfectly absorbing, so waves incident upon it are reflected with a reflection coefficient

$$\epsilon_R \equiv \frac{\delta\Sigma_R}{\delta\Sigma_{\text{out}}}. \quad (58)$$

Here, $\delta\Sigma_{\text{out}}$ is the amplitude of the outgoing wave (with respect to the BL), and $\delta\Sigma_R$ is the amplitude of the reflected wave. As long as ϵ_R is not close to 1, the reflected waves will not fundamentally affect the dynamics of the instabilities in the boundary layer, since the “overreflection” mechanism described in Belyaev & Rafikov (2012) only works if $\epsilon_R \approx 1$. However, the angular momentum current due to stresses measured by equation (49) will underestimate the true current, since the measured current contains components due to both the true outgoing waves (with respect to the BL) and the artificial reflected waves from the inner boundary. Nevertheless, the flux due to only the outgoing component, $C_{S,\text{out}}$, can be estimated in terms of the measured flux, $C_{S,\text{meas}}$, as

$$C_{S,\text{out}} = \frac{C_{S,\text{meas}}}{1 - \epsilon_R^2}. \quad (59)$$

This equation can be derived by considering a linear superposition of an outgoing wave and the reflected wave. The reflected wave has the opposite sign of C_S as the outgoing wave and an amplitude that is second order in ϵ_R , since angular momentum flux is a second order quantity.

Fig. 12a shows the measured current (black line) calculated using equation (49), and the analytically-predicted current due to waves (red line) calculated using equation (53). The analytically-

predicted current oscillates around the measured current, which is roughly constant for $\varpi \lesssim .96$. These oscillations can be explained by the presence of a reflected wave from the inner boundary with amplitude $\epsilon_R \approx .3$. This amplitude can be estimated from the straightforward-to-derive relation

$$\epsilon_R = \frac{C_{S,\max}^{1/2} - C_{S,\min}^{1/2}}{C_{S,\max}^{1/2} + C_{S,\min}^{1/2}}, \quad (60)$$

where $C_{S,\max}$ and $C_{S,\min}$ are the maximum and minimum values of the oscillations in the red, analytically predicted flux curve in Figure 12a.

The reason for the oscillations in the red curve of Fig. 12a is that equation (53) is an accurate estimator of the current due to waves if there are *only* outgoing waves present; it does not account for reflected waves. However, it is straightforward to modify equation (53) so that it estimates the current due to only the outgoing component. To do this, we assume that there is a single outgoing mode present with a constant value of k_ϖ that is reflected at the inner boundary into an incoming mode with the same value of k_ϖ and an amplitude which is a fraction ϵ_R of the amplitude of the outgoing mode. Under these assumptions, the current due to only the outgoing component, $C_{S,\text{out}}$, can be expressed in terms of the uncorrected current given by equation (53), $C_{S,\text{unc}}$, as

$$C_{S,\text{out}} = \frac{C_{S,\text{unc}}}{1 - 2\epsilon_R \cos(2k_\varpi \varpi + \psi) + \epsilon_R^2}, \quad (61)$$

where ψ is a free phase parameter.

The red curve in Fig. 12b shows $C_{S,\text{out}}$ as computed from equation (61), and the black curve shows $C_{S,\text{out}}$ according to equation (59). The oscillations in the red curve have all but disappeared after applying the correction to compute the flux from only outgoing waves. Moreover, the red and black curves are seen to be roughly constant for $\varpi \lesssim .96$ and to have very similar amplitudes. This proves that in the star, just as in the disk, angular momentum is carried away from the BL by waves. However, unlike in the disk, the waves do not shock as they penetrate into the star, but rather diminish in amplitude to conserve energy and angular momentum.

Comparing the scales on Figs. 9 and 12b, we see that the angular momentum flux into the star is larger than the angular momentum flux into the disk by an order of magnitude. This means that most of the angular momentum lost by the inner part of the disk goes into spinning up the star and only a small fraction is transported outward into the disk.

5.2. Lower Branch

We turn now to angular momentum transport for the lower branch. Fig. 13 shows C_S calculated using equation (49) for simulation 3D9e at time $t = 320$; the same time as Fig. 6b, when the lower branch is clearly dominant. Panel a of Fig. 13 depicts C_S from the inner edge of the simulation domain up to the inner edge of the evanescent region in the disk at $\varpi = 1.58$. Panel b,

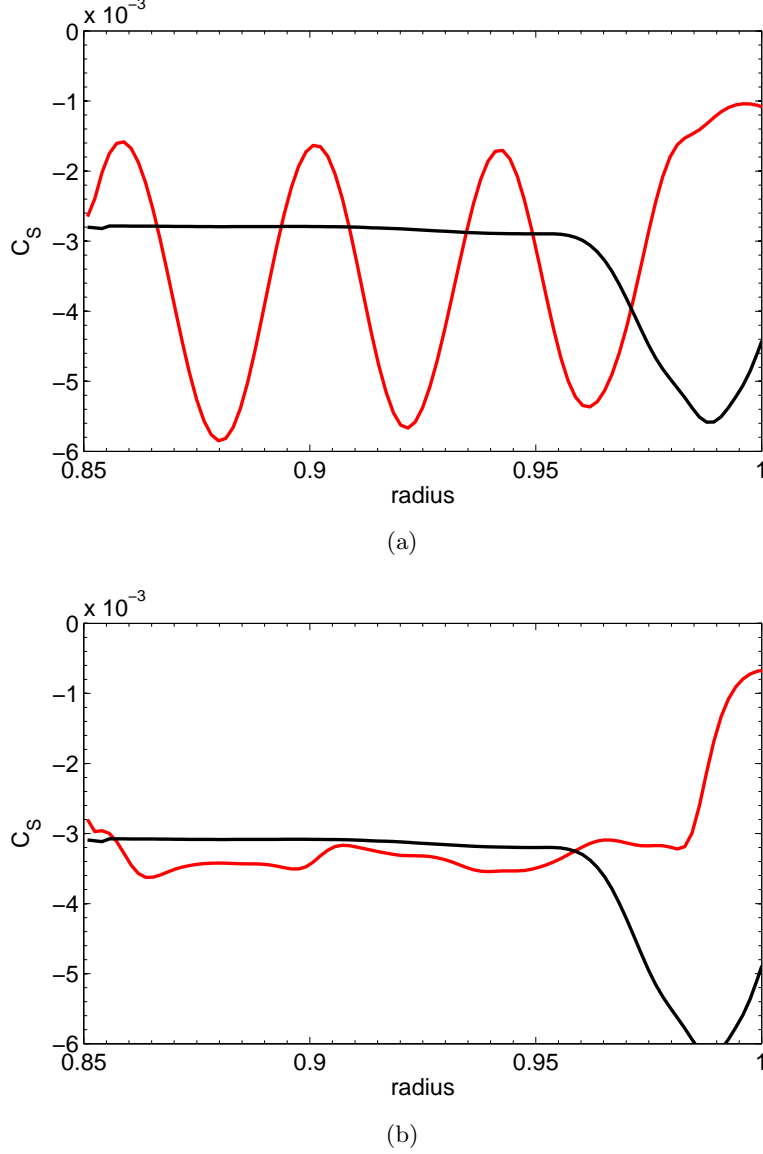


Fig. 12.— a) Uncorrected current due to stresses inside the star computed using equations (49) (black line) & (53) (red line). b) Corrected current due to outgoing waves computed using equations (59) (black line) & (61) (red line).

which has a different scale than panel a, depicts C_S from just inside the inner edge of the evanescent region to the outer edge of the simulation domain. The dashed lines in panel b depict the edges of the evanescent region, and the dotted line is the corotation radius ($\Omega_P \approx .42$). We point out that although the magnitude of C_S for the lower mode in Fig. 13 is smaller than the magnitude of C_S for the upper mode in Fig. 12, the amplitude of either mode is not constant in time. In fact the magnitude of C_S inside the star may be as high for the lower mode as for the upper mode at earlier

times (see Fig. 14 in §5.3).

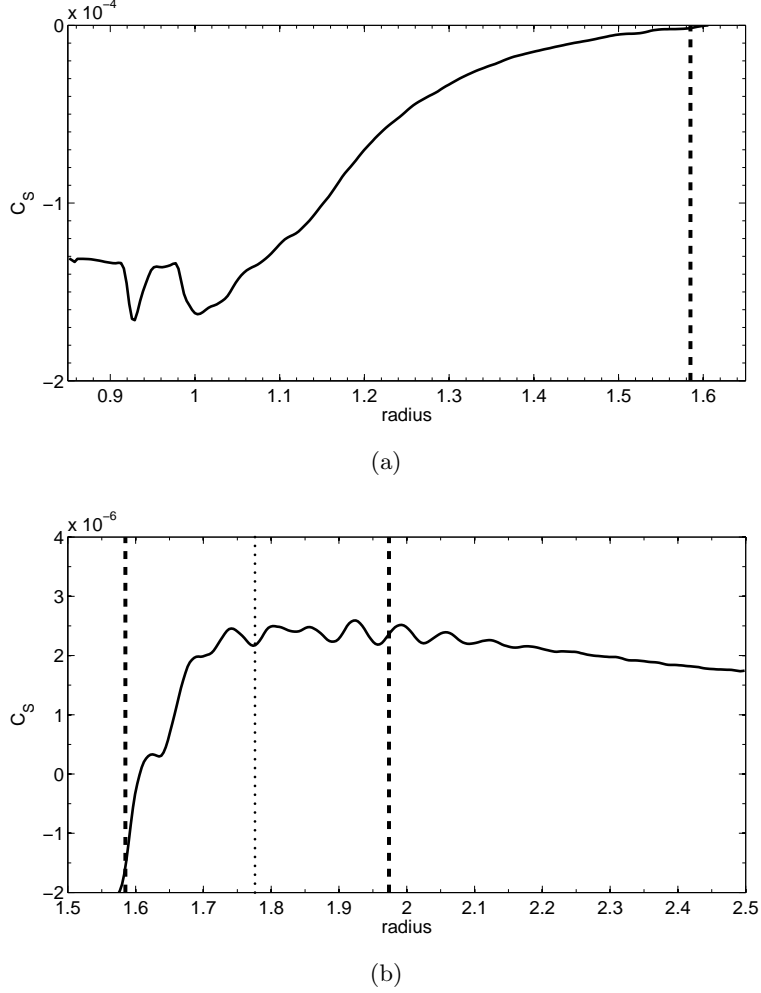


Fig. 13.— a) C_S for simulation 3D9e at time $t = 320$ inside the inner edge of the evanescent region in the disk. The dashed line marks the inner edge of the evanescent region in the disk b) Same as a, but C_S is shown within the evanescent region and beyond it. The evanescent region itself is located within the dashed lines and the dotted line is the corotation radius.

In contrast to the upper branch, it is more difficult to estimate the current due to waves using equations (54) and (53) in both the star and the disk for the lower branch. In the disk, the difficulty comes about due to the fact that there are both outgoing and reflected shocks between the surface of the star and the Lindblad resonance in the disk (Fig. 6b). Equation (54) only applies if there are exclusively outgoing waves, and it is not straightforward to modify it to account for interference effects from reflected waves. Without modification, the plot of the analytically predicted current, C_S , from equation (54) would show large spikes at shock crossings, and only in between shock crossings when the outgoing and reflected waves are well-separated is there reasonable agreement

between the measured and analytically predicted values of C_S (see Fig. 5 of Belyaev et al. (2012)).

The complication with applying equation (53) to analytically predict C_S inside the star is that $k_\varpi \approx 0$ (to zeroth order in M^{-1}) for the lower mode (§4.2.2), which makes the current estimated from equation (53) equal to zero. Thus, in order to use equation (53) we would need to know k_ϖ to first order in $1/M$, and we have chosen not to pursue such a calculation in this work.

One thing to notice in Fig. 13 is that C_S vanishes close to the edge of the evanescent region in the disk. This is to be expected if we have near perfect reflection, since $C_S = 0$ at the point of reflection if the amplitudes of the outgoing and reflected shocks are the same. $C_S \neq 0$ throughout the entire region between the BL and the inner edge of the evanescent region due to shock dissipation, which causes the shock amplitude, and consequently $|C_S|$, to diminish with increasing path length traveled by the shock. This makes $C_S < 0$ between the BL and the point of reflection, because the shock pattern has a negative angular momentum density inside corotation, and the outgoing shocks, which have a larger amplitude than the incoming ones, propagate in the $+\varpi$ direction.

We can estimate a lower bound on the reflection coefficient from the evanescent region by comparing the scales of Figs. 13a and 13b. The absolute value of C_S (for outgoing shocks only) is ~ 100 times lower outside the evanescent region than inside it. Since C_S is a second order quantity in $\delta\Sigma$, the reflection coefficient as defined in equation (58) is $\epsilon_R > .9$. This is only a lower bound on the reflection coefficient, since outside the evanescent region C_S could be dominated by an upper branch component.

We also point out that C_S changes sign within the evanescent region close to the corotation radius in the disk ($\varpi_{\text{CR}} = 1.78$), as expected for angular momentum transport by waves. C_S does not change sign at the corotation radius located in the BL at $\varpi \approx 1$, since both the direction of wave propagation, and the sign of the angular momentum density change there. In other words, inside corotation at $\varpi \approx 1$ the angular momentum density is positive, but waves propagate in the $-\varpi$ direction so $C_S < 0$. Just outside it, the angular momentum density is negative (since $\Omega_P < \Omega$ there), but waves propagate in the $+\varpi$ direction so $C_S < 0$ as well.

5.3. Relation of Angular Momentum Transport to Temporal Evolution

We now discuss how angular momentum transport in our simulations controls the temporal evolution of the system. One can use a characteristic value of $|C_S| \sim 3 \times 10^{-3}$ taken from Fig. 12 to estimate a typical “evolution time”, for the system when the upper branch is dominant. We define t_{evol} as the time it takes for the evanescent region (upper branch) in the disk to lose half its angular momentum. Taking the the evanescent region for upper branch to extend from $1 < \varpi < 1.25$, we estimate

$$t_{\text{evol}} \sim 300. \tag{62}$$

Fig. 14 shows a radius-time plot of C_S for simulation 3D9a. From the figure, it is clear that t_{evol} is within a factor of several of the span of time during which the upper branch is dominant. Moreover, we see as well from Fig. 14 that t_{evol} is also a good estimator of the timespan during which there is a significant angular momentum current radiated away from the BL and the accretion rate is highest.

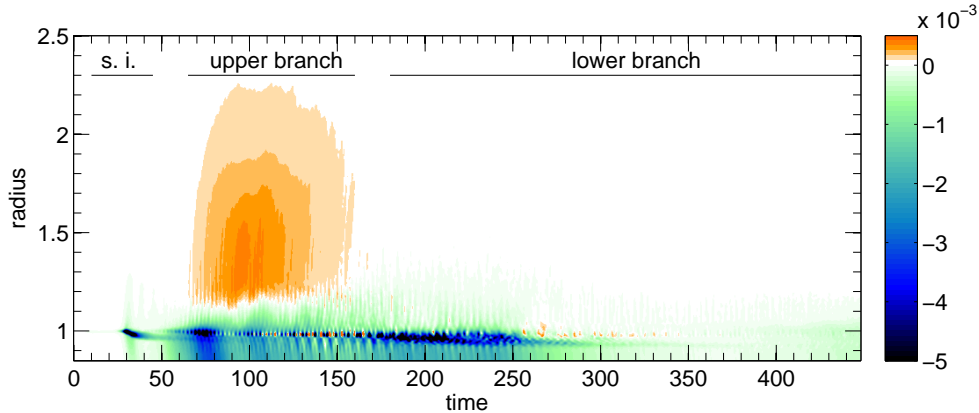


Fig. 14.— Radius-time image of C_S for simulation 3D9a. The horizontal bars show the periods of time when the sonic instabilities are active, the upper branch is dominant, and the lower branch is dominant.

The fact that the evolution time is comparable to both the timespan over which the upper branch is dominant and the timespan for significant mass accretion in the simulations suggests the following scenario for the temporal evolution of the system. The amplitude of the upper branch is initially high, but diminishes when it has depleted the evanescent region in the inner part of the disk of angular momentum. The system then switches to lower branch behavior with continuing mass accretion. However, without a mechanism of resupply for the inner disk, which does not exist in our simulations, the rate at which the inner disk is depleted of angular momentum must drop. Thus, the angular momentum current and the mass accretion rate both plummet for $t \gtrsim t_{\text{evol}}$ as seen in Figs. 1b and 14. This occurs in step with a reduction in the amplitude of the acoustic modes, which are responsible for the angular momentum transport.

In contrast to our simulations, there does exist a mechanism of resupply for the inner disk in an astrophysical system, namely accretion due to turbulent stresses. These stresses are not present in our simulation, since we do not have magnetic fields, which lead to the MRI instability in the disk. However, one may speculate that if the accretion time due to turbulent stresses were comparable to or shorter than t_{evol} , then the acoustic modes would operate at a high amplitude indefinitely. Indeed, the amplitude of the modes themselves could potentially be controlled by the time for MRI to resupply the inner part of the disk.

5.4. Relation of Angular Momentum Transport to Mass Accretion Rate

Angular momentum carried by the waves launched in the BL is eventually deposited into the disk fluid as a result of wave dissipation. In this section we relate the angular momentum transport rate to the mass accretion rate through the disk, \dot{M} , defined in equation (25).

We can use equations (15) and (16) to write \dot{M} in terms of C_S as

$$\dot{M} = \left[\frac{\partial}{\partial \varpi} (\Omega \varpi^2) \right]^{-1} \left[2\pi \varpi^3 \Sigma_0 \frac{\partial \Omega}{\partial t} + \frac{\partial C_S}{\partial \varpi} \right]. \quad (63)$$

Time evolution of Ω represented by the first term on the right hand side forces gas to move radially, since to conserve angular momentum fluid elements must readjust their radial distance, ϖ , when Ω varies. The $\partial \Omega / \partial t$ term in equation (63) vanishes for a steady state disk, but turns out to be important for our simulations, since the rotation profile evolves in time (Fig. 2).

We plot in Fig. (15) the mass accretion rate in the BL as a function of radius for simulation 3D9a averaged between times $t = 70 - 100$, when the upper mode with high Ω_P clearly dominates. The solid red and blue curves show the contributions of the $\partial C_S / \partial \varpi$ and $\partial \Omega / \partial t$ terms, respectively, to the mass accretion rate (equation [63]), as measured from the simulation, and the black curve shows the total mass accretion rate measured directly from the simulation using equation (25). It is clear that both the $\partial \Omega / \partial t$ and $\partial C_S / \partial \varpi$ terms contribute significantly to the mass accretion rate, even far out in the disk. As a consistency check, the sum of the solid red and blue curves is shown in purple and is seen to equal the black curve up to small wiggles that are artifacts of the measurement procedure.

Fig. 15 clearly shows that the $\partial \Omega / \partial t$ term is important for the calculation of \dot{M} . In our case, it is significant because the inner disk is depleted of mass as a result of angular momentum transport by acoustic modes. This causes time-varying density and pressure gradients in the disk, which is significant even quite far from the BL, at separations $\sim \varpi_*$ from it. Time evolution of this pressure support ultimately causes explicit time dependence of Ω and drives accretion even in the region where the wave has not shocked yet (interior to $\varpi \approx 1.8$ in Fig. 15).

Prior to its dissipation the wave propagating through the disk cannot affect its state (Goldreich & Nicholson 1989). Only after it shocks, transfer of its angular momentum to the disk drives additional mass accretion. The dashed red curve in Fig. 15 shows the theoretically predicted value for the component of mass accretion due to the $\partial C_S / \partial \varpi$ term in equation (63), assuming the $\partial C_S / \partial \varpi$ term is entirely due to shock dissipation. In other words, $\partial C_S / \partial \varpi$ is computed using equation (55), where we use equation (57) to calculate dE/dm , and measure $\Delta \Sigma / \Sigma$ in the same way described in §5.1.1. We point out that the formula for the $\partial C_S / \partial \varpi$ term due to shocks for the lower mode was given in Appendix B of Belyaev et al. (2012), and the derivation for the upper mode is nearly identical, see §5.

The good agreement between the solid and dashed red curves for $\varpi \gtrsim 1.8$ in Fig. 15 shows that the $\partial C_S / \partial \varpi$ component of the mass accretion rate is well-described by dissipation in shocks.

For smaller values of ϖ , the waves emitted from the BL have not yet fully shocked (§5.1.1), so the agreement is not as good.

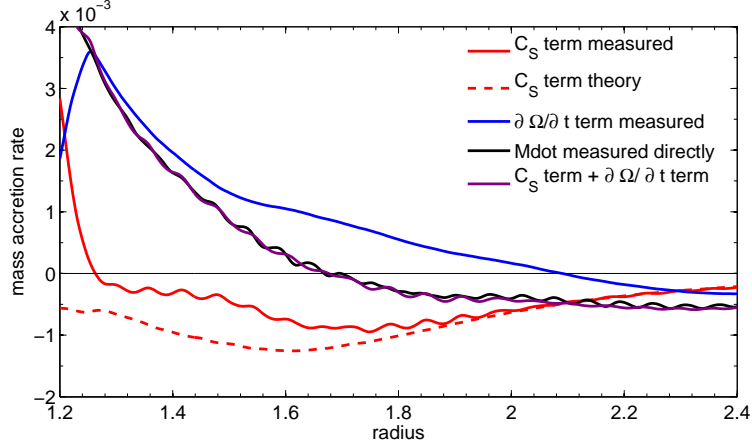


Fig. 15.— Plot of \dot{M} measured from the simulations (black line) and the contributions to \dot{M} from the $\partial C_S / \partial \varpi$ (solid red line) and $\partial \Omega / \partial t$ (blue line) terms in equation (63). The dashed red line shows the theoretical estimate for the $\partial C_S / \partial \varpi$ term assuming wave dissipation in shocks.

It is interesting to note that the mass accretion rate due to wave dissipation is negative in Fig. 15, i.e. the disk material is pushed away from the BL beyond the point where the wave has shocked. This is due to the fact that Fig. 15 corresponds to a time when the upper branch is dominant. As discussed in §4.2.1, the upper branch has a fast pattern speed with a corotation radius in the disk at $\varpi_{\text{cr}} \approx 1.12$ for this simulation. Outside of corotation ($\varpi > \varpi_{\text{cr}}$), $\Omega_P > \Omega$ so the wave has a positive angular momentum density. Thus, dissipation of the wave *increases* the angular momentum of the fluid elements in the disk, causing them to move *outwards* and resulting in a *negative* mass accretion rate.

The situation is different for the lower and middle branches. Unlike the upper branch which has an evanescent region directly adjacent to the boundary layer, the middle and lower branches have their evanescent regions in the disk separated from the boundary layer. Waves can propagate between the BL and the evanescent region in the disk. Since $\Omega_P < \Omega$ in this region, this implies that the wave has *negative* angular momentum density and dissipation of the wave results in a *positive* mass accretion rate. Beyond the evanescent region in the disk, $\Omega_P > \Omega$ for both the lower and middle branches so the mass accretion rate due to wave dissipation is in principle negative in this region, just as for the upper branch. However, very little flux penetrates the evanescent region (§5.2), so the contribution to mass accretion from wave dissipation beyond the evanescent region in the disk is very small for the lower and middle branches.

6. Effect of Stratification on Acoustic Modes

Up to now we have discussed the results of unstratified simulations, and we find that *density* stratification does not produce fundamentally different behavior. In particular, the upper, lower, and middle branches are all observed in stratified simulations, as well, and facilitate angular momentum transport.

Panels a and b of Fig. 16 show snapshots of the upper and lower branches for simulation 3D9c at times $t = 160$ and $t = 320$ in the color variable $\varpi\sqrt{\Sigma}\langle v_{\varpi}\rangle_z$. Comparing Fig. 16 with Fig. 6, we see that the spatial morphology of the wave branches is the same in the stratified and unstratified cases. In addition, we showed in §4 that the dispersion relations (32) (upper branch), (38) (lower branch), and (42) (middle branch) provided a good estimate of the pattern speed in simulations irrespective of stratification. Thus, we conclude that stratification has little effect on the dynamics and morphology of the modes for an isothermal equation of state.

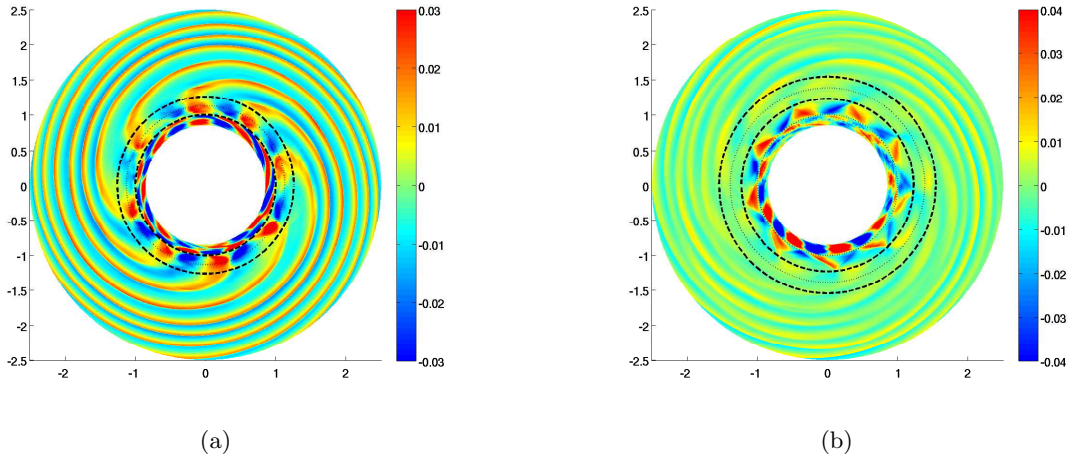


Fig. 16.— Panels a and b show snapshots of $\varpi\sqrt{\Sigma}\langle v_{\varpi}\rangle_z$ when the upper and lower waves are dominant, respectively, although there appears to be a superposition of both types of waves in the panels. The dashed and dotted circles depict the boundaries of evanescent regions and corotation radii, respectively. In panel a, the evanescent region in the disk extends all the way to the BL.

Although stratified and unstratified simulations exhibit similar behavior, there are some obvious differences. For instance, in stratified simulations we observe the formation of a neck in the density profile, which is shown in Fig. 17. The formation of this neck implies that sonic instabilities operate preferentially near the equator and spin up an equatorial belt on the star.

Further evidence in favor of a spun up equatorial belt can be seen in Fig. 18, which shows contours of the density-weighted azimuthal average of v_{ϕ} at $t = 0$ (panel a) and $t = 150$ (panel b). It is clear from panel b that the equatorial region of the star is spinning faster than higher latitudes. For an isothermal equation of state or more generally for any equation of state that is a function of

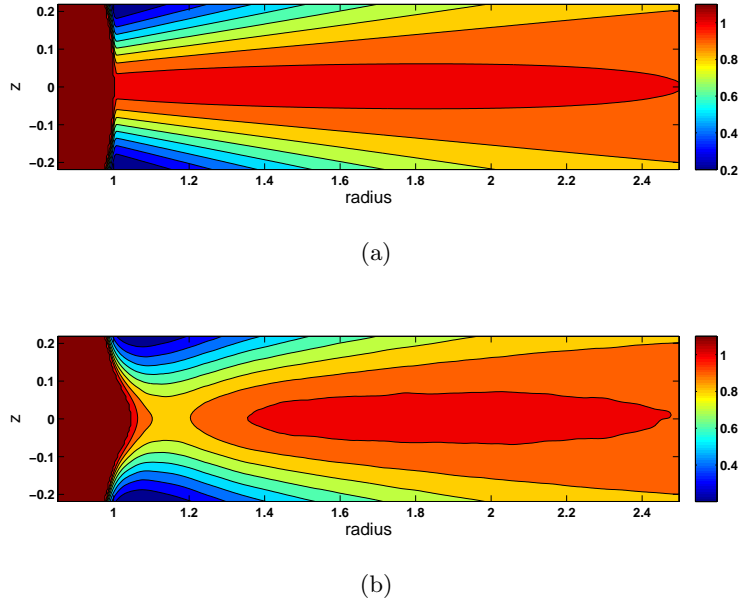


Fig. 17.— Panels a and b show contours of the azimuthally-averaged density profile at $t = 0$ and $t = 150$, respectively, for simulation 3D9c. Formation of a neck in the density distribution is clearly visible in panel b.

the pressure alone, deviation from rotation on cylinders as see in Fig. 18b implies the existence of meridional circulation. Thus, although we do not see evidence of significant azimuthal spreading of disk material over the surface of the star, we do observe the sonic instabilities to induce meridional flows.

In principle, one may also interpret the vertical extent of the equatorial bulge of the spun-up fluid in our stratified simulations as evidence for the emergence of a spreading layer (Inogamov & Sunyaev 1999; Piro & Bildsten 2004a) on the stellar surface. However, given the simplified nature of our runs (e.g. isothermal EOS), it difficult to unambiguously claim observation of this phenomenon in the simulations.

Another difference between stratified and unstratified simulations is that t_{evol} as defined in equation (62) is a factor of two or so higher in the stratified case. This implies that the acoustic modes have lower amplitudes and take a longer time to transport angular momentum away from the inner disk in the stratified case. Thus, mass accretion and angular momentum transport can occur at an appreciable rate for a longer time before shutting off when the inner disk has been depleted of material (§5.3).

Panels a and b of Fig. 19 show radius-time plots of $\langle v_{\varpi} \rangle$ and C_S , respectively, for the stratified simulation 3D9c. These radius-time plots can be compared with those for the unstratified case shown in Figs. 1b and 14. Both the unstratified and stratified radius-time plots look fundamentally

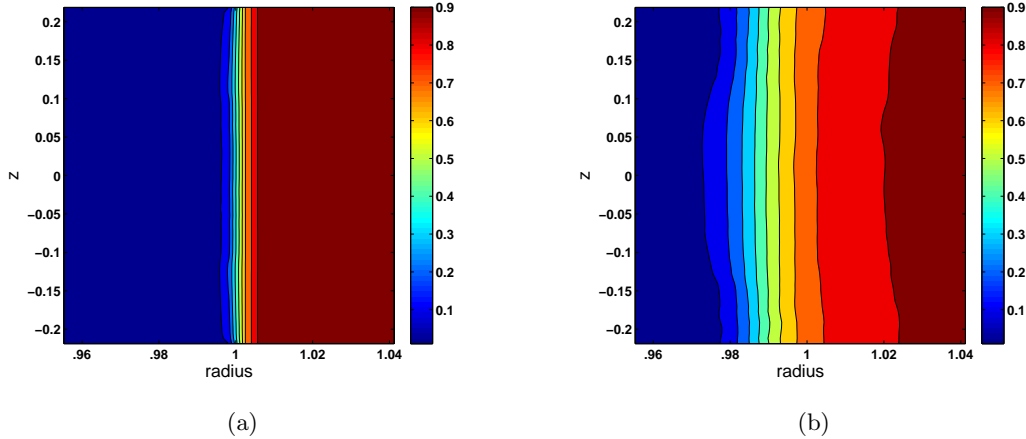


Fig. 18.— Panels a and b show contours of the density-weighted azimuthal average of v_ϕ at $t = 0$ and $t = 150$, respectively, for simulation 3D9c. There is a slight deviation from rotation on cylinders in panel b with the equatorial plane rotating faster than higher latitudes.

similar. However the features in the stratified simulation appear to be “stretched” in time as compared to the unstratified one, providing evidence that t_{evol} is longer in the stratified case.

7. The Incompatibility of α Models and Angular Momentum Transport by Waves

As we have shown, angular momentum transport in our simulations is facilitated by quasi-2D acoustic waves, rather than turbulent stresses. This assertion follows from the fact that C_S is well-described by theoretical formulas applicable for waves §5.1, and that most of the power in the fluctuations is in $k_z = 0$ modes §4.4. Because α -models are based on the notion of a local effective viscosity due to turbulent stresses, whereas waves are inherently nonlocal, transporting angular momentum over long distances before they are absorbed or dissipate, it is clear that any conventional model of α viscosity is inapplicable to the BL.

We can make this point more concrete with three specific reasons why an α model is not applicable to transport by waves. First, in conventional α models the stress vanishes (and C_S changes sign) when $\partial\Omega/\partial\varpi = 0$, and this is not observed in our simulations. Instead, in a wave model, the stress vanishes (and C_S changes sign) when $\Omega = \Omega_P$, and we do see evidence of this (see §5.1.1 and 5.2). Although there is a corotation resonance in the BL, which could in principle be located close to the point where $d\Omega/d\varpi = 0$, this is a fundamentally different criterion. Moreover, for waves there is another corotation resonance in the disk, where C_S changes sign, which is an effect not captured by α models.

Second, equations (53) and (54), which describe transport by waves are fundamentally different in structure from equations (26)-(28) and depend on quantities such as $\Delta\Sigma/\Sigma$ and Ω_P . The former

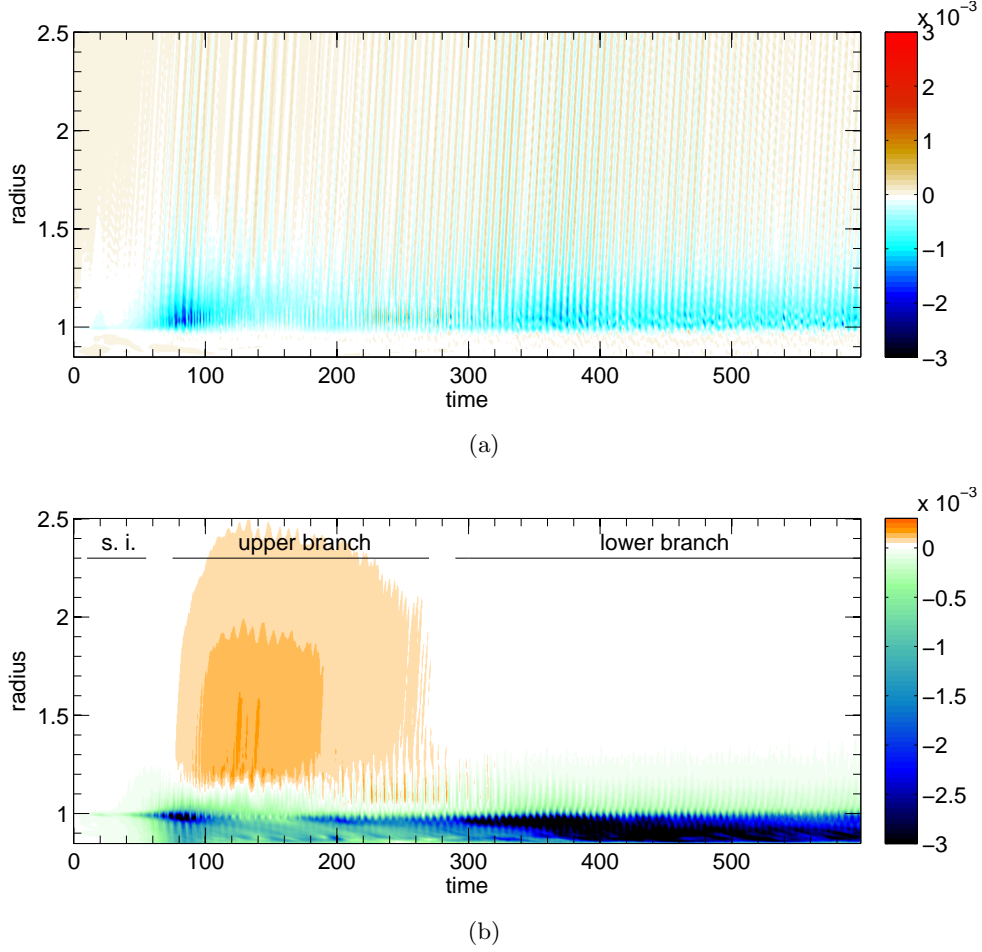


Fig. 19.— Panels a and b show radius-time plots of $\langle v_{\varpi} \rangle$ and C_S for simulation 3D9c.

is a function of time that depends in a complicated way on the details of the sonic instability, and the latter depends on the particular wave branch. Thus, although possible, it would be contrived to boil down an expression containing these quantities into an effective viscosity parameter; any such parameter would be a complicated function of the wave branch (upper, lower, or middle), azimuthal wavenumber, wave amplitude, Mach number, radius, etc.

Third, Navier Stokes viscosity with an enhanced value of the viscosity coefficient, ν , due to turbulence assumes *local* transport of angular momentum, which is the reason why the stress is proportional to $\partial\Omega/\partial\varpi$. When angular momentum is carried by waves over long distances, the transport is *nonlocal* — different parts of the disk can exchange angular momentum only when waves dissipate, which often happens at large separation from their launching site. Thus any model, such as α viscosity, which is based on Navier-Stokes viscosity no longer applies. The possibility of non-local momentum transport has been hinted at by Inogamov & Sunyaev (2010), who postulated that angular momentum transport within the spreading layer (a BL with substantial extent in the

θ direction) of a neutron star occurs by wave damping, in order to avoid excessive heating at the base of the layer.

For these reasons, we believe it is better to use equations (53) and (54) as they are for estimating angular momentum transport in the BL. We do not provide an effective α for our simulations, since it is incorrect to adopt an α viscosity model when angular momentum is transported by waves.

8. Discussion

The major result of this work is a new picture of the momentum, energy, and mass transfer in astrophysical BLs. We have found that the isothermal boundary layer naturally supports three $k_z = 0$ branches of acoustic modes when there is a supersonic velocity drop across it. These three types of acoustic modes are directly related to the three types of waves found for the isothermal vortex sheet in Belyaev & Rafikov (2012). Each of the three acoustic mode wave branches is associated with a different spatial morphology. However, two features common to all of the wave branches are emission of sound waves from the BL into both the star and the disk and the presence of two corotation radii – one within the disk and the other within the BL. The corotation radius within the disk lies inside a broad evanescent region (see Fig. 6).

The behavior of a particular mode is affected by the density stratification inside the star and the differential rotation inside the disk. The latter can potentially lead to the formation of a pattern of trapped shocks inside a resonant cavity in the disk near the BL. For this to occur, the inner edge of the evanescent region inside the disk must be well-separated from the BL.

An important point is that the dispersion relations for all three acoustic mode wave branches remain the same in 2D, 3D unstratified, and 3D stratified simulations. This can be seen from Tables 2 & 3 and Figure 5. Thus, the proposed picture of angular momentum transport in the BL is robust with respect to the dimensionality of the problem, strengthening the results previously obtained by Belyaev et al. (2012).

An acoustic mode with pattern speed Ω_P couples to fluid at the corotation radius within the BL ($\Omega(\varpi_c) = \Omega_P$), sapping it of angular momentum and driving accretion onto the central object. Thus, the fluid in the BL loses angular momentum to waves, which propagate away from the BL.

A fraction of the angular momentum radiated away from the BL is redeposited in the disk by wave dissipation in shocks, which drive the evolution of the disk surface density (§5.4). An additional factor in the time-evolution of the disk surface density is the time-dependence of Ω , which is connected with the temporal evolution of the radial pressure gradient in the disk. The time-dependence of Ω is an important effect in our naturally-evolving simulations. However, in a truly steady-state model of the BL, this contribution to the temporal evolution of the disk surface density would be absent.

The remainder of angular momentum lost by fluid in the BL is radiated into the star. Waves

propagating away from the BL and into the star weaken in amplitude as a result of angular momentum conservation in a medium with a rising density. For this reason, waves inside the star do not shock — their nonlinear evolution is too weak and in our simulations they simply propagate out through the inner boundary of the simulation domain. In a real system, they would presumably be damped by some *linear* dissipation process such as conduction or radiation, ultimately transferring their angular momentum and energy to the star.

The radiation of angular momentum by waves away from the BL and its subsequent redistribution by damping of these waves are manifestly nonlocal processes, see §7. This casts serious doubt on the utility of semi-analytic models employing an (intrinsically local) α -prescription for viscosity in predicting BL structure and observational manifestations.

The general picture of acoustic wave-mediated BL dynamics advanced in this work may potentially have several important consequences that we discuss next. We warn, however, that until simulations with a more realistic equation of state are performed, some of the following predictions may be somewhat speculative.

8.1. Implications: Energy Transport in the BL

Waves propagating away from the BL carry not only angular momentum but also energy, which is released by accreting material as it is spun down. Wave damping in the disk or star results in the *nonlocal* release of this accretion energy — energy is deposited into the disk or star *at the location where the wave damps*. For example, the rate of thermal energy release in the disk per unit radial distance due to dissipation of waves with pattern speed Ω_P is

$$\frac{\partial \dot{E}_d}{\partial \varpi} = [\Omega_P - \Omega(\varpi)] \frac{\partial C_S}{\partial \varpi}, \quad (64)$$

where $\partial \dot{E}_d / \partial \varpi$ denotes the energy dissipation rate per unit radius (i.e. $(\partial \dot{E}_d / \partial \varpi) d\varpi$ is the energy dissipated in an annulus between ϖ and $\varpi + d\varpi$). By our definition, which is consistent with the definition in §6.4.2 of Binney & Tremaine (2008), $\dot{E}_d \leq 0$ and is non-zero only where $\partial C_S / \partial \varpi \neq 0$, (i.e. after the wave has shocked in the disk). This non-local energy transport may affect the structure and observational manifestations of the BL in the following way.

Conventional wisdom based on local α -models (e.g. Balsara et al. (1999)) states that the intense energy release has to take place in the BL itself, heating the gas there and considerably modifying the structure of the BL. This does not need to be true in our picture of wave-mediated transport: kinetic energy of material accreting through the BL can be transported away from the layer by waves and deposited in both the disk and the star. This can easily prevent the layer from overheating, meaning that its structure may be affected by accretional energy dissipation *weaker* than was thought before. This is a very important consequence of wave-driven transport.

Unfortunately, we cannot explore the effect of nonlocal energy transport on BL structure in

our simulations directly, since they employ an isothermal equation of state and may not accurately capture the details of wave dissipation, especially inside the star. However, the removal of accretion energy from the BL in the form of waves that is a prediction of our model adds some support to the results of our purely isothermal simulations, which assume the fluid temperature does not change at all.

As we have seen in §5.1, at least during some periods of time $|C_s|$ going into star is much larger than that going into the disk. Since the energy density of a wave is directly proportional to its angular momentum density, $E_w = \Omega_P L_w$ (Binney & Tremaine 2008), it is natural to expect that most of the accretional energy released in the BL is ultimately deposited in the star, rather than in the disk. As a result, heating of disk material by wave dissipation, which is distributed over a radial range $\Delta\varpi \sim \varpi_\star$ is unlikely to exceed the energy release in the inner disk due to conventional anomalous viscosity, such as MRI. The latter does not operate in our simulations since we have focused on the pure hydro case. Thus, if acoustic waves dominate transport in the BL one might expect the effective temperature of the inner disk and its overall spectrum *not to change much* compared to models not accounting for the presence of a BL, which seems to be precisely what is observed in some systems (Ferland et al. 1982; Polidan et al. 1990).

Depending on the nature of the accreting object, deep heating occurring inside the star as a result of wave dissipation may affect its internal structure. This effect is likely to be minimal for white dwarfs and neutron stars, which are supported by degeneracy pressure, but may be important for accreting pre-main sequence stars. Indeed, a typical T Tauri star accreting at the rate $\dot{M} = 10^{-6} M_\odot \text{ yr}^{-1}$ (typical during the so-called FU Orionis outbursts) should have a rate of accretional energy release in the BL comparable to its own luminosity $\sim L_\odot$. Depending on the depth at which the waves excited in the BL dissipate, the nonlocal energy transport into the star may be able to affect its structure (Prialnik & Livio 1984; Hartmann et al. 1997; Popham 1997). In fact, Kenyon et al. (1988) and Popham et al. (1996) have previously shown that during FU Orionis outbursts, T Tauri stars may increase their radii by a factor ~ 2 , which might be explained in our model by accretional energy release inside the star mediated by acoustic waves.

Observational signatures of the BL should also be affected by nonlocal transport of energy in the form of waves. Accretional energy carried away by waves is either buried in the star or transferred to the disk, both of which affect the spectrum of the BL. Given that wave dissipation is expected to only mildly heat the inner disk above its standard temperature set by the visco-turbulent heating rate (Shakura & Sunyaev 1973), it may even be natural that the spectrum of the system will have a rather weak contribution from the BL as most of the liberated energy is buried in the star. In the case of protostellar accretion, the sequestration of accretional energy released during FU Orionis outbursts inside the star may help explain the so-called “luminosity problem” — an apparent discrepancy between the expected accretion luminosities of protostars and their observed luminosities (Kenyon et al. 1990; Evans et al. 2009). BL formation is expected during FU Orionis outbursts with their high value of \dot{M} , which allows the disk to overcome magnetic truncation. A sizeable fraction of the energy released during these intense bursts of accretion can

then be deposited deep inside the star by dissipation of acoustic modes. This energy would later leak out of the star, on a timescale which is of the order of the thermal timescale at the depth where the energy carried by waves is deposited.

The same process could potentially explain why BL emission is missing from some observations of accreting systems (Ferland et al. 1982; Polidan et al. 1990). In this framework, existing observations of high-energy spectral excesses from accreting systems, such as cataclysmic variables (Pandel et al. 1987), conventionally ascribed to BL emission, may in fact be due to some sort of coronal emission produced above the inner disk. Hard X-ray excesses found in accreting neutron star systems can be due to emission from a spreading layer (Gilfanov et al. 2003; Revnivtsev & Gilfanov 1984), which has a different morphology from the BL.

8.2. Implications: stellar spinup

Deposition of angular momentum carried by waves deep into the star will cause stellar spinup to occur in a non-trivial fashion — angular momentum will be added to the star where waves dissipate, spinning up the inner parts of the star, which are hidden from direct view. As a result, the surface layers of the star may rotate *slower* than would be expected if the angular momentum of accreted material were deposited locally, near the BL. Unfortunately, we cannot directly explore this issue in detail in our simulations due to their simplified nature.

Previously Barker & Ogilvie (2010) have proposed a similar picture of inside-out stellar spinup by dissipation of tidally excited internal gravity waves near the stellar center. Clearly, this mode of stellar spinup is quite different from the predictions of standard BL models based on the notion of local α -viscosity (Kippenhahn & Thomas 1978).

8.3. Implications: mixing in the BL

The standard paradigm of local viscosity in the BL generally assumes that angular momentum transport in the BL is facilitated by turbulence resulting from nonlinear saturation of some local instability such as Kelvin-Helmholtz (Kippenhahn & Thomas 1978; Inogamov & Sunyaev 2010), baroclinic (Piro & Bildsten 2007), etc. Quite naturally, turbulence in the layer would also result in efficient mixing of fluid elements, leading to elemental homogeneity if different parts of the layer have different chemical compositions.

The situation is different if transport in the layer is facilitated by acoustic modes as we find in this work. Wave-driven transport in the supersonic case does not need an exchange of fluid elements to occur and thus does not necessarily result in efficient mixing inside the layer. This agrees with what we generally find in our simulations, which typically exhibit large-scale regular structures like the pattern of trapped shocks and show very little evidence for small-scale turbulence that would

efficiently mix the layer. Thus, one may expect elemental mixing to be less prominent in our picture of the BL, compared to conventional models.

Having said that we point out that previously Belyaev et al. (2012) found using 2D simulations that the regular pattern of fluid motion in the vicinity of the layer can be occasionally interrupted by the short-term bursts of very irregular, rather turbulent behavior, which might result in efficient mixing of the layer. However, we do not observe such bursts in our 3D simulations, possibly because in 3D as opposed to 2D, our simulations do not develop an inflection point in the rotation profile within the BL. This important issue clearly needs further study.

8.4. Implications: variability of emission

Another implication of transport by waves is that they naturally produce temporal variability, since a pattern of acoustic modes rotating at a well-defined pattern speed invariably leads to periodic emission from the BL. Note that this mechanism of variability is completely different from previous suggestions such as a non-axisymmetric bulge in the disk near the BL (Popham 1999) or shallow surface waves on a spreading layer (Piro & Bildsten 2004b), which can provide additional sources of variability.

Our simulations do not implement radiative transfer and thus cannot directly link periodicity of fluid patterns to spectral variability of the BL. Nevertheless, temporal behavior of the BL has the potential to provide the most direct link between our work and observations, since from our dispersion relations for the upper, middle, and lower branches it is possible to work out the *frequency spectrum* of the BL. It is clear that it should feature a peak at frequency $\omega = m\Omega_P$, which corresponds to the apparent periodicity of the wave pattern to an external observer.

In our simulations, we typically find quite high values of $\omega = m\Omega_P \sim (4 - 6)\Omega(\varpi_*)$ for the most commonly observed pattern of trapped lower branch modes. Moreover, from equation (39), we have the following lower bound for the frequency of the lower branch $m\Omega_P > M\Omega(\varpi_*)/2$. This lower bound makes it unlikely that acoustic modes (or at the very least the lower mode, which is prevalent at late times in our simulations) can explain the origin of dwarf novae oscillations (DNOs) in cataclysmic variables (Warner 2004), which typically have $M \sim 100$ and $m\Omega_P \lesssim \Omega(\varpi_*)$ (Patterson 1981).

On the other hand, the nature of our simulations may prevent us from seeing all possible sources of variability in the BL. In particular, a well known peculiarity of the isothermal equation of state used in this work is that the Brunt-Väisälä frequency

$$N^2 = (\gamma - 1) \frac{g^2}{s^2} \quad (65)$$

is zero if $\gamma = 1$. This means that gravity waves (*g*-modes) in the star are neutrally buoyant ($\omega = 0$) and thus do not show up in our simulations.

A more realistic equation of state having $\gamma > 1$ would be able to support both acoustic modes (p -modes) and gravity waves (g -modes) inside the star. The latter correspond to the lower (“–”) sign in the dispersion relation (34) and have lower frequency than acoustic modes, potentially making them relevant for explaining DNOs. In principle, density waves in the disk could couple to both g -modes and p -modes in the star, whereas only the latter coupling is possible for the isothermal equation of state. Thus, a real BL would likely support more than just the three acoustic wave branches described in this work and Belyaev & Rafikov (2012), and the dispersion relation for gravity modes in the star coupled to density waves in the disk remains to be worked out.

8.5. Future prospects

Our study employs two crucial simplifying assumptions: an isothermal EOS and lack of magnetic fields. Relaxing the first assumption requires using a more realistic EOS and properly characterizing radiation transfer in the system. In addition to previously mentioned consequences — e.g. appearance of new modes, see §8.1 & 8.4 — a better treatment of thermodynamics will have other implications.

For example, damping of modes excited in the BL depends on thermodynamics: it was previously shown by e.g. Lubow & Ogilvie (1998), Bate et al. (2002) that *thermal* stratification results in wave action channeling towards the low density regions, which may accelerate the nonlinear evolution of modes and cause them to damp faster. This would affect the dissipation pattern of waves, bringing disk regions where wave energy and momentum are deposited closer to the BL and making the BL more pronounced from an observational point of view. Additionally, compressional heating of accreted material in the BL can promote the formation of a spreading layer (Inogamov & Sunyaev 1999; Piro & Bildsten 2004a) on the surface of the accreting object.

Inclusion of magnetic field in our calculations should also have interesting consequences. First, it would result in the presence of MRI within the disk, which will provide a means of mass delivery from the outer disk to the BL region. At the moment, during the periods of lower mode dominance in our simulations, the fluid outside of the evanescent region in the disk remains unaffected by acoustic modes. As a result, mass depleted from the innermost disk does not get replenished by external accretion. Second, MRI would introduce turbulent motions in the disk, which may interact with the BL modes in a non-trivial fashion and enhance the importance of $k_z \neq 0$ modes for angular momentum transport within the disk. Third, the number of possible wave branches the system could support would be even higher in the MHD case, since the disk would be able to support slow, fast, and Alfvén waves, which could couple to p and g -modes in the star. Finally, field amplification by intense shear in the BL would affect the internal dynamics of the layer. We leave the detailed exploration of these issues to future study.

Resources supporting this work were provided by the NASA High-End Computing (HEC)

Program through the NASA Advanced Supercomputing (NAS) Division at Ames Research Center. We thank Jeremy Goodman and Anatoly Spitkovsky for useful discussions. The financial support for this work is provided by the Sloan Foundation and NASA grant NNX08AH87G.

REFERENCES

- Armitage, P. J. 2002, MNRAS, 330, 895
- Balbus, S. A., & Hawley, J. F. 1991, ApJ, 376, 214
- Balbus, S. A., & Papaloizou, J. C. B. 1999, ApJ, 521, 650
- Balsara, D. S., Fisker, J. L., Godon, P., & Sion, E. M. 2009, ApJ, 702, 1536
- Barker, A. J. & Ogilvie, G. I. 2010, MNRAS, 404, 1849
- Bate, M. R., Ogilvie, G. I., Lubow, S. H., & Pringle, J. E. 2002, MNRAS, 332, 575
- Belyaev, M. A., & Rafikov, R. R. 2012, ApJ, 752, 115
- Belyaev, M. A., Rafikov, R. R., & Stone, J. M. 2012, arXiv:1205.4009
- Binney, J., & Tremaine, S. 2008, Galactic Dynamics: Second Edition, by James Binney and Scott Tremaine. ISBN 978-0-691-13026-2 (HB). Published by Princeton University Press, Princeton, NJ USA, 2008.
- Cowling, T. G. 1941, MNRAS, 101, 367
- Evans, N. J. II, Dunham, M. M., Jorgensen, J. K., et al. 2009, ApJS, 181, id. 321
- Ferland, G. J., Pepper, G. H., Langer, S. H., et al. 1982. ApJ, 262, L53
- Gerwin, R. A. 1968, Reviews of Modern Physics, 40, 652
- Ghosh, P., & Lamb, F. K. 1978, ApJ, 223, L83
- Gilfanov, M. & Revnivtsev, M., & Molkov, S. 2003, A&A, 410, 217
- Glatzel, W. 1988, MNRAS, 231, 795
- Goldreich, P., & Nicholson, P. D. 1989, ApJ, 342, 1075
- Goldreich, P., & Tremaine, S. 1978, ApJ, 222, 850
- Hartmann, L., Cassen, P., & Kenyon, S. J. 1997, ApJ, 475, 770
- Inogamov, N. A., & Sunyaev, R. A. 1999, Astronomy Letters, 25, 269

- Inogamov, N. A., & Sunyaev, R. A. 2010, *Astronomy Letters*, 36, 848
- Kenyon, S. J., Hartmann, L., & Hewett, R. 1988, *ApJ*, 325, 231
- Kenyon, S. J., Hartmann, L. W., Strom, K. M., & Strom, S. E. 1990, *AJ*, 99, 869
- Kippenhahn, R. & Thomas, H.-C. 1978, *A&A*, 63, 265
- Kluźniak, W. 1987, Ph.D. Thesis, Stanford University
- Landau, L. D., & Lifshitz, E. M. 1959, *Course of theoretical physics*, Oxford: Pergamon Press, 1959
- Larson, R. B. 1990, *MNRAS*, 243, 588
- Lubow, S. H. & Ogilvie, G. I. 1998, *ApJ*, 504, 983
- Miles, J. W. 1958, *Journal of Fluid Mechanics*, 4, 538
- Miles, J. W. 1961, *Journal of Fluid Mechanics*, 10, 496
- Narayan, R., Goldreich, P., & Goodman, J. 1987, *MNRAS*, 228, 1
- Pandel, D., Córdova, F. A., Mason, K. O., & Priedhorsky, W. C. 2005, *ApJ*, 626, 396
- Papaloizou, J. C. B., & Pringle, J. E. 1984, *MNRAS*, 208, 721
- Patterson, J. 1981, *ApJS*, 45, 517
- Pessah, M. E., & Chan, C.-k. 2012, *ApJ*, 751, 48
- Piro, A. L., & Bildsten, L. 2004, *ApJ*, 610, 977
- Piro, A. L., & Bildsten, L. 2004, *ApJ*, 616, L155
- Piro, A. L., & Bildsten, L. 2007, *ApJ*, 663, 1252
- Polidan, R. S., Mauche, C. W., & Wade, R. A. 1990, *ApJ*, 356, 211
- Popham, R. 1997, *ApJ*, 478, 734
- Popham, R. 1999, *MNRAS*, 308, 979
- Popham, R., & Narayan, R. 1995, *ApJ*, 442, 337
- Popham, R., Kenyon, S., Hartmann, L., Narayan, R. 1996, *ApJ*, 473, 422
- Prialnik, D. & Livio, M. 1985, *MNRAS*, 216, 37
- Revnivtsev, M. G. & Gilfanov, M. R. 2006, *A&A*, 453, 253

Shakura, N. I., & Sunyaev, R. A. 1973, A&A, 24, 337

Stone, J. M., Gardiner, T. A., Teuben, P., Hawley, J. F., & Simon, J. B. 2008, ApJS, 178, 137

Vallis, G. K., *Atmospheric and Oceanic Fluid Dynamics*, Cambridge University Press, 2006

Warner, B. 2004, PASP, 116, 115

Zingale, M., Dursi, L. J., ZuHone, J., et al. 2002, ApJS, 143, 539

A. Dispersion Relation for Loosely Wound Modes Having $m \gg 1$ in the Disk

We derive here the dispersion relation for loosely wound modes having $m \gg 1$ in an isothermal disk (equation [32]). We assume a two dimensional setup in the ϖ - ϕ plane and ignore stratification. Thus, we replace the density ρ by the surface density Σ .

We start by explicitly writing the continuity and momentum equations in cylindrical coordinates (e.g. Binney & Tremaine (2008)), along with the isothermal equation of state. We denote the radial and azimuthal velocities by u and v respectively

$$\frac{\partial \Sigma}{\partial t} + \frac{1}{\varpi} \frac{\partial}{\partial \varpi} (\varpi \Sigma u) + \frac{1}{\varpi} \frac{\partial}{\partial \phi} (\Sigma v) = 0 \quad (\text{A1})$$

$$\frac{\partial u}{\partial t} + u \frac{\partial u}{\partial \varpi} + \frac{v}{\varpi} \frac{\partial u}{\partial \phi} - \frac{v^2}{\varpi} = -\frac{\partial \Phi}{\partial \varpi} - \frac{1}{\Sigma} \frac{\partial P}{\partial \varpi} \quad (\text{A2})$$

$$\frac{\partial v}{\partial t} + u \frac{\partial v}{\partial \varpi} + \frac{v}{\varpi} \frac{\partial v}{\partial \phi} + \frac{vu}{\varpi} = -\frac{1}{\varpi} \frac{\partial \Phi}{\partial \phi} - \frac{1}{\Sigma \varpi} \frac{\partial P}{\partial \phi} \quad (\text{A3})$$

$$P = \Sigma s^2 \quad (\text{A4})$$

Next, we assume a constant equilibrium disk density, which through the equation of state implies a constant equilibrium disk pressure. We also ignore self-gravity so there is no perturbation to the potential. Specifying first order quantities with a preceding δ , the linearized momentum and continuity equations then become

$$\frac{\partial \delta \Sigma}{\partial t} + \Omega \frac{\partial \delta \Sigma}{\partial \phi} + \frac{\Sigma}{\varpi} \frac{\partial \delta v}{\partial \phi} + \frac{\Sigma}{\varpi} \delta u + \Sigma \frac{\partial \delta u}{\partial \varpi} = 0 \quad (\text{A5})$$

$$\frac{\partial \delta u}{\partial t} + \Omega \frac{\partial \delta u}{\partial \phi} - 2\Omega \delta v + \frac{1}{\Sigma} \frac{\partial \delta P}{\partial \varpi} = 0 \quad (\text{A6})$$

$$\frac{\partial \delta v}{\partial t} + \Omega \frac{\partial \delta v}{\partial \phi} + \frac{\partial(\varpi \Omega)}{\partial \varpi} \delta u + \Omega \delta u + \frac{1}{\Sigma \varpi} \frac{\partial \delta P}{\partial \phi} = 0 \quad (\text{A7})$$

$$\delta P - s^2 \delta \Sigma = 0 \quad (\text{A8})$$

Taking perturbations in the form $\exp[i \int^\varpi d\varpi' k_\varpi(\varpi') + im(\phi - \Omega_P t)]$ and eliminating δP in favor of $\delta\Sigma$, the linearized set of equations becomes

$$im(\Omega - \Omega_P) \frac{\delta\Sigma}{\Sigma} + \frac{1}{\varpi}(1 + in)\delta u + \frac{im}{\varpi}\delta v = 0 \quad (\text{A9})$$

$$im(\Omega - \Omega_P)\delta u - 2\Omega\delta v + \frac{is^2n}{\varpi} \frac{\delta\Sigma}{\Sigma} = 0 \quad (\text{A10})$$

$$im(\Omega - \Omega_P)\delta v + \frac{\kappa^2}{2\Omega}\delta u + \frac{is^2m}{\varpi} \frac{\delta\Sigma}{\Sigma} = 0, \quad (\text{A11})$$

where we have defined

$$n(\varpi) \equiv \varpi k_\varpi, \quad (\text{A12})$$

and used the epicyclic frequency

$$\kappa^2 = 2\Omega \left(2\Omega + \varpi \frac{d\Omega}{d\varpi} \right). \quad (\text{A13})$$

We can eliminate δv in equations (A9) and (A10) by using (A11) to arrive at

$$i \left[m^2(\Omega - \Omega_P)^2 - \frac{s^2m^2}{\varpi^2} \right] \frac{\delta\Sigma}{\Sigma} - \frac{m}{\varpi} \left[\frac{\kappa^2}{2\Omega} - (1 + in)(\Omega - \Omega_P) \right] \delta u = 0 \quad (\text{A14})$$

$$\left[m^2(\Omega - \Omega_P)^2 - \kappa^2 \right] \delta u - \frac{s^2m}{\varpi} [2\Omega i - n(\Omega - \Omega_P)] \frac{\delta\Sigma}{\Sigma} = 0. \quad (\text{A15})$$

After some algebra, the above system of equations reduces to

$$\left[m^2(\Omega - \Omega_P)^2 - \frac{s^2m^2}{\varpi^2} \left(1 + \frac{n^2}{m^2} - i \frac{n}{m^2} \right) - \kappa^2 \right] + \frac{is^2}{\varpi^2(\Omega - \Omega_P)} \left[-2\Omega(i - n) - \frac{n\kappa^2}{2\Omega} \right] = 0. \quad (\text{A16})$$

We now make the approximations $m \gg 1$ and $n/m \ll 1$, and we shall refer to the latter as the “loose winding” approximation. In that case, equation (A16) can immediately be simplified to

$$\left[m^2(\Omega - \Omega_P)^2 - \frac{s^2m^2}{\varpi^2} - \kappa^2 \right] + \frac{is^2}{\varpi^2(\Omega - \Omega_P)} \left(-2\Omega(i - n) - \frac{n\kappa^2}{2\Omega} \right) = 0. \quad (\text{A17})$$

We see that the term in the square brackets is the dispersion relation (32). Therefore, it is left to show that the other terms are negligible. To start, note that if we take in order of magnitude $\kappa \sim \Omega$, then the “other” terms are in order of magnitude

$$\frac{1}{m(\Omega - \Omega_P)} \left[\kappa \frac{s^2m^2}{\varpi^2} \max \left(\frac{1}{m}, \frac{n}{m} \right) \right]. \quad (\text{A18})$$

It is straightforward to show that regardless of whether $\kappa \gg sm/\varpi$, $\kappa \ll sm/\varpi$, or $\kappa \sim sm/\varpi$ the term in equation (A18) is smaller than $m^2(\Omega - \Omega_P)^2$ (and hence the dominant terms in the square brackets in equation (A17)) by a factor of *at least*

$$\max \left(\frac{1}{m}, \frac{n}{m} \right) \ll 1. \quad (\text{A19})$$

Thus, as long as $m \gg 1$ and $n/m \ll 1$, the dispersion relation is accurately given by equation (32). In our simulations $10 < m < 40$, so the first of these conditions is typically well-satisfied. It is more difficult to get a handle on how well the “loose winding” condition is satisfied. However, the fact that Table 2 shows that there is agreement between theory and simulations at the several percent level is good justification for the use of equation (32).

B. Dispersion Relation for an Isothermal Stratified Atmosphere in Cylindrical Geometry

We consider the dispersion relation for an unrotating stratified atmosphere in cylindrical geometry. Our aim is to justify our use of equation (38), which is valid for plane-parallel geometry. For simplicity, we assume two-dimensional perturbations in the $\varpi - \phi$ plane. However, we do not initially specify the form of the gravitational potential $\Phi(\varpi)$, only specifying it when necessary to make the calculations tractable.

As in Appendix A, we start with equations (A1)-(A4). We take small perturbations on top of the equilibrium state, and again denote small first order quantities with a preceding δ . The linearized forms of the continuity and momentum equations and the equation of state are then given by

$$\frac{1}{\Sigma} \frac{\partial \delta \Sigma}{\partial t} - h_s^{-1} \delta u + \frac{1}{\varpi} \frac{\partial}{\partial \varpi} (\varpi \delta u) + \frac{1}{\varpi} \frac{\partial \delta v}{\partial \phi} = 0 \quad (\text{B1})$$

$$\frac{\partial \delta u}{\partial t} + \frac{1}{\Sigma} \frac{\partial \delta P}{\partial \varpi} + s^2 h_s^{-1} \frac{\delta \Sigma}{\Sigma} = 0 \quad (\text{B2})$$

$$\frac{\partial \delta v}{\partial t} + \frac{1}{\Sigma \varpi} \frac{\partial \delta P}{\partial \phi} = 0 \quad (\text{B3})$$

$$\delta P - s^2 \delta \Sigma = 0, \quad (\text{B4})$$

where we have defined

$$h_s(\varpi) \equiv - \left(\frac{1}{\Sigma} \frac{d\Sigma}{d\varpi} \right)^{-1} \quad (\text{B5})$$

to be the local scale height of the atmosphere.

We now assume perturbations in the form $f(\varpi) \exp[i(m\phi - \omega t)]$. Eliminating $\delta \Sigma$ and δv from equations (B1)-(B4) we have

$$-i\omega \frac{\delta P}{P} + \left[\frac{1}{\varpi} \left(1 - \frac{\varpi}{h_s} \right) + \frac{\partial}{\partial \varpi} \right] \delta u + i \left(\frac{m^2}{\varpi^2} \right) \frac{s^2}{\omega} \frac{\delta P}{P} = 0 \quad (\text{B6})$$

$$-i\omega \delta u + \frac{s^2}{P} \frac{\partial \delta P}{\partial \varpi} + \frac{s^2}{h_s} \frac{\delta P}{P} = 0. \quad (\text{B7})$$

Finally, eliminating δu in terms of δP we arrive at the second order differential equation in terms

of $\delta P/P$

$$\left(\frac{\omega^2}{s^2} - \frac{m^2}{r^2}\right) \frac{\delta P}{P} + \left(1 - \frac{\varpi}{h_s}\right) \frac{1}{\varpi} \frac{\partial}{\partial \varpi} \left(\frac{\delta P}{P}\right) + \frac{\partial^2}{\partial \varpi^2} \left(\frac{\delta P}{P}\right) = 0. \quad (\text{B8})$$

We can gain insight by comparing the differential equation (B8) to the second order equation for $\delta P/P$ in the plane-parallel case for constant gravity with stratification in the x -direction. The latter is given by Vallis (2006) as

$$\left(\frac{\omega^2}{s^2} - k_y^2\right) \frac{\delta P}{P} - \frac{1}{h_s} \frac{\partial}{\partial x} \left(\frac{\delta P}{P}\right) + \frac{\partial^2}{\partial x^2} \left(\frac{\delta P}{P}\right) = 0. \quad (\text{B9})$$

Equation (B8) reduces *locally* to equation (B9) at a given radius $\overline{\varpi}$ in the limit

$$\frac{h_s(\overline{\varpi})}{\overline{\varpi}} \ll 1, \quad (\text{B10})$$

if we make the association $k_y \rightarrow m/\overline{\varpi}$. In our simulations, $h_s/\varpi \sim .02$, so the condition (B10) is well-satisfied. The local equivalence of equations (B9) and (B8) thus provides a justification for our use of an effective radius in the dispersion relation (38).

C. Dissipation Rate in the Isothermal Limit

We derive here a formula for the energy dissipation per unit mass due to a shock in the isothermal limit, $\gamma \rightarrow 1$. This is important in the context of our simulations, since the entropy is not well-defined if $\gamma = 1$. This can be seen from the expression for the entropy per unit mass for an ideal gas

$$\frac{dS}{dm} = \frac{s^2}{T\gamma(\gamma-1)} \ln(P\rho^{-\gamma}) \quad (\text{C1})$$

is ill-defined if $\gamma = 1$.

The energy dissipation rate of the wave used in equation (55) for an isothermal shock¹ is given by

$$\frac{dE}{dm} = T\Delta \frac{dS}{dm} \quad (\text{C2})$$

where the Δ denotes the difference in a quantity across the shock. It is important to show that $\Delta dS/dm$ and hence dE/dm converges to a well-defined value when $\gamma \rightarrow 1$. We perform this below, and derive an exact result for the dissipation rate dE/dm in the isothermal limit. Larson (1990)

¹An isothermal shock means that the temperature is the same on either side of the shock but not necessarily that $\gamma = 1$.

has given an approximate expression for dE/dm valid for arbitrary γ in the limit of weak shocks. We note that our exact expression (equation [57]) matches the expression of Larson (1990) when $\gamma = 1$ (equation [56]) to leading order (third) in $\Delta\Sigma/\Sigma$.

To start, we combine equations (C1) and (C2) to write

$$\frac{dE}{dm} = \frac{s^2}{\gamma(\gamma - 1)} \ln \left[\frac{P_1}{P_0} \left(\frac{\rho_1}{\rho_0} \right)^{-\gamma} \right], \quad (\text{C3})$$

where the subscripts “0” and “1” denote pre and postshock quantities respectively. Using the Rankine-Hugoniot relations and defining $\gamma = 1 + \delta$ and $\epsilon \equiv \rho_1/\rho_0 - 1$, equation (C3) becomes

$$\frac{dE}{dm} = \frac{s^2}{(1 + \delta)\delta} \ln \left[\frac{2 + \epsilon(2 + \delta)}{2 - \epsilon\delta} (1 + \epsilon)^{-(1+\delta)} \right]. \quad (\text{C4})$$

Next, we take the isothermal limit $\delta \rightarrow 0$ and expand the expression inside the logarithm in powers of δ . Equation (C4) then becomes

$$\frac{dE}{dm} = \frac{s^2}{(1 + \delta)\delta} \ln \left[1 + \left(\frac{\epsilon(2 + \epsilon) - (1 + \epsilon) \ln(1 + \epsilon)}{2(1 + \epsilon)} \right) \delta + \mathcal{O}(\delta^2) \right]. \quad (\text{C5})$$

Expanding the logarithm in powers of δ and keeping the highest order term we arrive at equation (57)

$$\frac{dE}{dm} = s^2 \frac{\epsilon(2 + \epsilon) - 2(1 + \epsilon) \ln(1 + \epsilon)}{2(1 + \epsilon)}. \quad (\text{C6})$$

Note that this expression is valid for all values of ϵ .